Ultrafast spin and heat transport after femtosecond pulsed laser excitation in metals

Verhoeven, W.

Award date:
2013

Eindhoven University of Technology
Department of Applied Physics
Physics of Nanostructures group (FNA)

Ultrafast Spin and Heat Transport After Femtosecond Pulsed Laser Excitation in Metals

Wouter Verhoeven

August 2013

Supervisors:
A.J. Schellekens, M.Sc.
prof.dr. B. Koopmans

Abstract

In this thesis electron and spin transport are investigated on sub-picosecond timescales. This is done by measuring the influence of transport on the demagnetization of a magnetic material after heating by a short laser pulse.

Two different effects have been examined. First, it was investigated whether spin transport can have a large influence on the laser-induced demagnetization of a ferromagnetic thin film, which has been proposed recently. This is done by measuring the demagnetization of a nickel thin film placed on both a conducting and an insulating substrate. We have shown that the measurements can not be explained by spin transport, and that processes that locally dissipate spin momentum are therefore dominant. No signs of spin transport have been found in nickel, although due to the uncertainty of the measurements a small influence of spin transport on the magnetization dynamics can not be excluded.

The second part of this thesis focusses on the control of heat transport by using a so-called spin-valve geometry. The heat conduction of such a spin-valve can be altered using a magnetic field. The demagnetization of a magnetic layer placed on top of the spin-valve was then measured, and it has been unambiguously shown that the demagnetization is affected by this change in heat conduction. With this a proof of concept has been provided for the control of ultrafast heat transport. Furthermore, simulations were done on the device using different models to describe heat transport. These simulations show that the size of the measured effect approximately corresponds to expectations.

Contents

Chapter 1

Introduction

Ever since the discovery of Mott that an electron current can be divided into two separate channels, one for spin-up and one for spin-down electrons, researchers have been looking for ways to utilize this spin property. An important step in this field of spintronics was made by Fert in 1988 and Grünberg in 1989, who both separately discovered the giant magnetoresistance effect, which causes the resistance of a device to change depending on an externally applied magnetic field. Thanks to this discovery huge progress was made in the development of read heads for magnetic data storage devices, resulting in an increase in storage density for these devices over the last couple of decades that surpasses even Moore's law.[1]

However, hard disks are starting to reach their maximum capabilities, and research is slowly shifting towards other devices, such as the magnetic random access memory[2] and the so-called racetrack memory.[3] Both again exploit the spin property of an electron, using magnetoresistive junctions to store bits, or using domain walls which can be moved by current-induced torques respectively. Both of these technologies offer higher read and write speeds, larger storage densities, and virtually a complete resistance to physical shocks.

Besides data storage, the future of spintronics looks even more promising, allowing a large variety of technologies ranging from simple logic devices or low-power transistors to the more exotic quantum computers. However, much is still unknown about manipulating the spin property, making spintronics both technologically and scientifically a very interesting and highly relevant field of research.

The goal of the research presented in this thesis is to investigate spin dynamics on sub-picosecond timescales. One of the questions addressed in this thesis is whether the manipulation of spins can be used to control heat transport through a device on these timescales. This could prove to be useful for the recently invigorated field

of spin caloritronics, where the spin degree of freedom is employed to improve on thermoelectric devices such as heat sensors or waste heat recyclers. Furthermore, this allows for new devices in which the role of transport on ultrafast magnetization dynamics can be investigated.

In the following part of this chapter, a short introduction will be given to the branch of spintronics most relevant to the research presented in the rest of this thesis, namely that of manipulating spins on extremely short timescales. At the end of this chapter the main goals of the thesis are presented, and a small outline of all the following chapters is given.

1.1 Ultrafast Magnetization Dynamics

Fast switching of the magnetization of a magnetic layer is a necessity for magnetic storage devices. This switching is usually accomplished using either a magnetic field, or with a current exerting a torque on the magnetization. Since both require the magnetization to switch through a precessional motion, both are limited to a minimum timescale. This minimum time required is typically several hundreds of picoseconds, both for magnetic field[4,5] and spin torque switching.[6]

However, a third possibility is to use ultrashort laser pulses to change the magnetization. By heating the magnetic material with a laser, the magnetization will decrease. This is shown in Fig. 1.1 (a), where the temperature dependence of the magnetization is plotted. By using ultrashort laser pulses, typically several tens of femtoseconds, the magnetization can be fully quenched within a picosecond. If this is now done with a ferrimagnetic material, the magnetization can reverse due to this heating, opening up the possibility of THz writing rates.[7]

The ultrafast quenching of the magnetization was first discovered in 1996 by Beaurepaire *et al*,[8] who measured the magnetization of a nickel thin film at a certain time after heating with a laser pulse. However, they found not only a decrease of the magnetization within a picosecond, but also a slightly slower recovery over several picoseconds, as is shown in Fig. 1.1 (b). This was explained by dividing the total system into three interacting subsystems, i.e. an electron, spin and lattice system. Each of these system has its own temperature, as shown in Fig. 1.1 (c). After the electron system absorbs heat from the laser pulse, the spin temperature will quickly equilibrate with the suddenly increased electron temperature, resulting in the fast demagnetization. The lattice will then absorb part of the heat from the other two systems on larger timescales until a complete equilibrium is reached, resulting in the slower recovery of part of the magnetization.

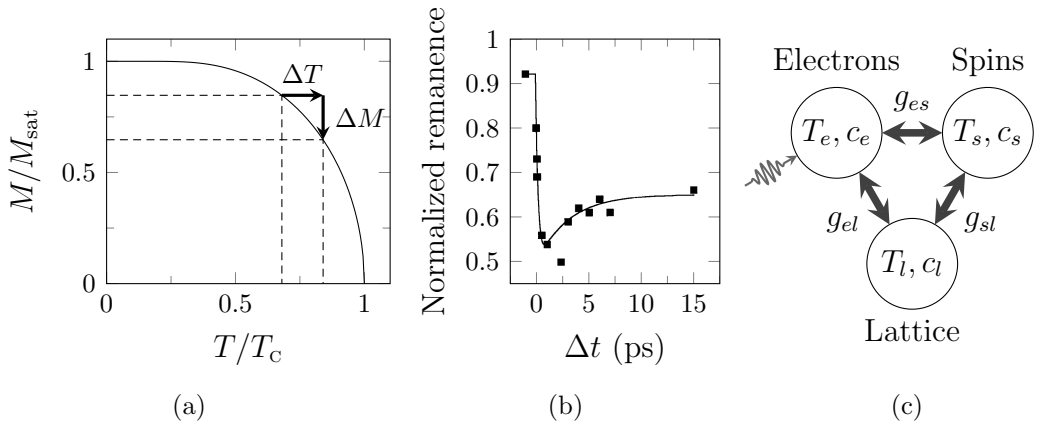

Figure 1.1: (a) Typical temperature dependence of the magnetization. Due to heating by the laser, the magnetization will decrease. (b) Magnetic remanence as a function of time as measured by Beaurepaire *et al.*, reprinted from Ref. 8. (c) Model used to explain the demagnetization. The complete system is divided into three subsystems, each having its own temperature and specific heat. The three systems exchange energy through their coupling constants g.

1.2 Ultrafast Transport

With this phenomenological description the demagnetization could be accurately described, and in the years following the discovery it was therefore universally believed that the demagnetization results from heating of the system, although the microscopic origin of the fast demagnetization is still under debate. In 2010 Koopmans *et al.* proposed a model where quenching of the magnetization results from spin flip scattering events.[9] This model could not only explain the results found by Beaurepaire *et al.*, but also the much larger demagnetization times found in materials such as gadolinium.

However, another model was also presented in 2010 by Battiato *et al.*, where the measured demagnetization was no longer described by heating of the material, but by superdiffusive transport of the excited electrons.[10,11] This transport results in a spin current directed away from the surface. The total magnetization will then remain the same, but a smaller magnetization is measured due to the finite penetration depth of the laser, which is approximately tens of nanometers.

The fact that transport plays an important role for the demagnetization can be seen in Fig. 1.2 (a) and (b), where the demagnetization of a single perpendicularly magnetized Co / Pt layer placed on top of a second similar Co / Pt layer is measured for both a parallel and an antiparallel alignment. If the two layers

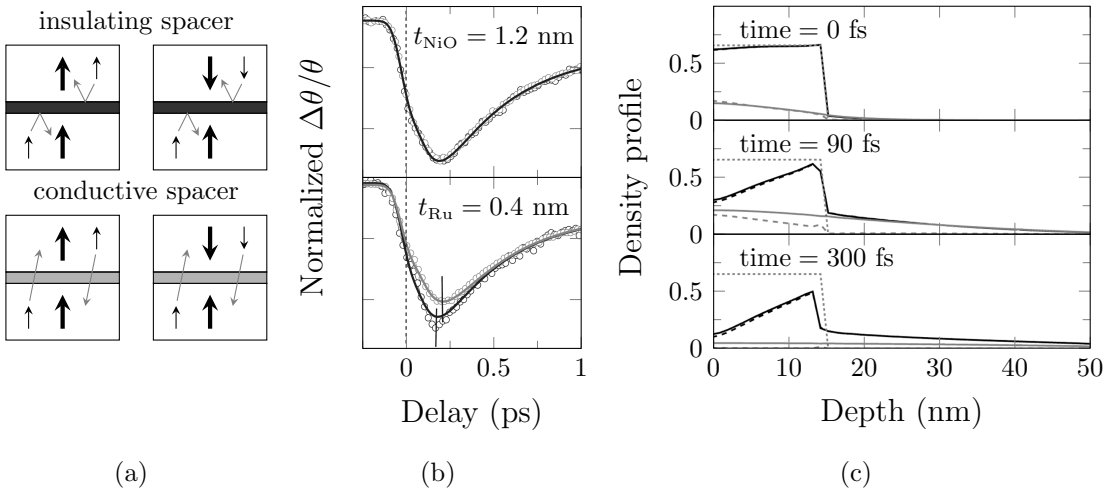

Figure 1.2: (a) Schematic diagram of the experiment by Malinowski *et al.* to measure spin angular momentum transfer between two magnetic layers. (b) Measured demagnetization of the top layer in the case of parallel (gray) and antiparallel (black) alignment, and in case of either an insulating NiO or a conducting Ru spacer layer. Data from Ref. 12. (c) Calculated spatial spin densities due to superdiffusive transport of electrons. Only the solid black lines are of interest, which show the total magnetization. Data from Ref. 10.

are separated by a thin insulating NiO layer, spin transport between the layers is blocked and both alignments show a similar demagnetization. However, if a conducting Ru spacer layer is used, the electrons of the two layers can interact, providing an extra channel of spin angular momentum transfer in the case of antiparallel alignment. This results in an increase in magnetization and a decrease in characteristic demagnetization time, both of $\sim 25\,\%$.

Since transport plays an important role at these length- and timescales, Battiato *et al.* proposed a model where the demagnetization is caused by a redistribution of the excited electrons. After electrons are excited by the laser, the majority spins travel through a magnetic material much easier. If the material is placed on top of a conducting substrate, majority electrons are then more likely to move into the substrate, leaving an excess of minority carriers behind. If this effect is strong enough, a lower magnetization will be measured purely due to this transport. Figure 1.2 (c) shows the results of simulations done with this model, where the magnetization is plotted at three different times after laser excitation.

The question now arises if transport of electrons is indeed strong enough to be the main driving force of the demagnetization. One of the goals of the research presented in this thesis is to investigate whether this is the case.

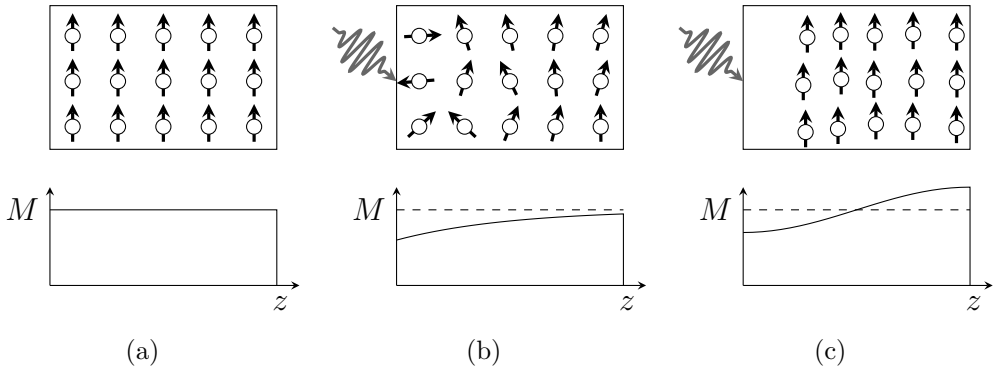

Figure 1.3: Spin distribution and magnetization as a function of depth (a) before heating, and after heating for (b) a model based on local dissipation of spin angular momentum and (c) a model based on spin transport. Due to the different magnetization profiles, a clear distinction can be made between the two models if the demagnetization is measured from both sides.

1.3 This Thesis

In this thesis the influence of both spin and heat transport on ultrafast magnetization dynamics is investigated. The main goal of investigating spin transport is to see whether the large influences on the demagnetization as proposed by Battiato *et al.* are indeed present. This is done by measuring the demagnetization of a nickel thin film placed on top of an insulating substrate. Measurements were done while heating from both the front and the back, which is expected to offer a clear distinction between the two models. The reason for this is that the superdiffusive model predicts an increase in magnetization when heating from the other side due to the excited electrons piling up at the surface of the device, while a decrease is expected in a model of local demagnetization. This is schematically illustrated in Fig. 1.3. Furthermore, the superdiffusive transport model predicts an enhanced demagnetization when a conducting substrate is used. Therefore measurements were also done on a nickel thin film placed on top of an aluminum layer.

The second goal is to see if heat transport inside the device can be controlled through magnetic ordering. This is done using the so-called giant magnetothermal resistance effect. This effect causes the heat conduction of two magnetic layers to depend on their relative alignment. By placing a third layer with a perpendicular magnetization on top of these two layers, a different demagnetization is then expected depending on the heat conduction, providing insight in both the possibility of controlling transport on ultrafast timescales, and its influence on the demagnetization process. Figure 1.4 shows a rough representation of this experiment.

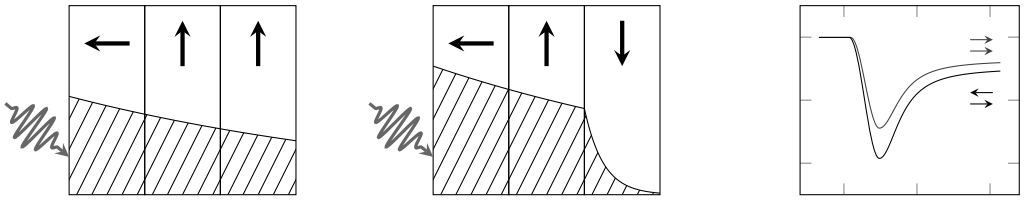

(a) (b) (c)

Figure 1.4: Temperature profile inside the device in (a) parallel and (b) antiparallel configurations. Due to the giant magnetothermal resistance effect, the heat conduction of the parallel configuration is higher. Because of this, more heat is expected to flow out of the top layer after laser excitation, resulting in a smaller demagnetization, as shown in (c).

This report consists of 7 chapters. The following outline shortly summarizes the contents of each chapter.

Chapter 2: Theory. In this chapter all theory relevant to the measurements is presented.

Chapter 3: Methods. In this chapter the experimental setup is presented, together with the measuring procedure.

Chapter 4: Investigating Spin Transport. Here, all results are presented that were done to investigate whether spin transport plays a dominant role for the demagnetization process. These results show no sign of spin transport, showing that local dissipation of spin angular momentum is the dominant process in nickel thin films.

Chapter 5: Simulations. In this chapter all the simulations on heat transport are presented. The goal of these simulations is mainly to get a rough estimate of how large an effect can be achieved, and how the device can be optimized.

Chapter 6: Controlling Heat Transport. Here, the fabrication steps of the device are presented, after which all measurements done on the final device are discussed. These results show that it is indeed possible to control heat transport using a spin-valve device.

Chapter 7: Conclusions and Outlook. Finally, all important conclusions are summarized, and some ideas for future research on this subject are presented.

Chapter 2

Theory

In this chapter, all theory relevant to the experiments will be introduced. First, two models are presented, one to explain the temperature dependence of the magnetization inside a ferromagnetic material, and one to explain the demagnetization process. Next, some important properties of transport are presented. The GMR and GMTR effects are explained first, and then transport on ultrafast timescales is discussed. Finally, the equations used to calculate the amount of light absorbed by a dielectric material are presented.

2.1 Ferromagnetism

Inside a ferromagnetic material there is an interaction between the electrons that will cause them to prefer to align their spin. This interaction is called the exchange interaction, and has a similar effect on the electrons as an external magnetic field. According to the Weiss mean field model the exchange interactions of a single spin with all other spins can therefore be approximated as a single average exchange field. This effective field is proportional to the magnetization, or

$$\mathbf{H}_{\text{ex}} = \lambda \mathbf{M} \,. \tag{2.1}$$

The Weiss constant λ is determined by the strength of the exchange interaction.

This effective magnetic field will cause the energy levels of an atom to shift due to Zeeman splitting. The energy shift of each level is given by

$$U = -\boldsymbol{\mu} \cdot \mathbf{B} = m_J g \mu_{\text{B}} \mu_0 H \,, \tag{2.2}$$

with $\boldsymbol{\mu}$ the magnetic moment of the atom, m_J the azimuthal quantum number, g the Landé factor and μ_{B} the Bohr magneton, which is approximately equal to the

magnetic moment of a free electron. The atom will thus have a lower energy if its magnetic moment aligns with the magnetic field.

Because of this energy splitting the occupation of these levels in thermal equilibrium will change. In the case of only two levels, the population of each level in the presence of a magnetic field can be evaluated using Boltzmann statistics:[13]

$$\begin{aligned} \frac{N_\uparrow}{N} &= \frac{\exp(\mu B/k_\mathrm{B}T)}{\exp(\mu B/k_\mathrm{B}T)+\exp(-\mu B/k_\mathrm{B}T)} \\ \frac{N_\downarrow}{N} &= \frac{\exp(-\mu B/k_\mathrm{B}T)}{\exp(\mu B/k_\mathrm{B}T)+\exp(-\mu B/k_\mathrm{B}T)} \,. \end{aligned} \tag{2.3}$$

For paramagnetic materials these populations are equal in the absence of an external magnetic field. However, for ferromagnetic materials the exchange field will create an excess of spins in one direction, giving rise to a magnetization. By combining equations (2.1)–(2.3) the magnetization can be written as

$$M = (N_\uparrow - N_\downarrow)\mu = M_\mathrm{sat} \tanh\left(\frac{M}{M_\mathrm{sat}}\frac{T_\mathrm{C}}{T}\right) , \tag{2.4}$$

where $M_\mathrm{sat} = N\mu$ is the saturation magnetization, and T_C the Curie temperature, given by

$$T_\mathrm{C} = \tfrac{1}{2} g \mu_\mathrm{B} \mu_0 \lambda M_\mathrm{sat}/k_\mathrm{B} \,.$$

Equation (2.4) only has a solution for $T < T_\mathrm{C}$. If a ferromagnetic material is heated above the Curie temperature, the magnetic ordering is thus lost.

If the atom now has an angular momentum quantum number J it will attain $2J+1$ equally spaced energy levels due to the splitting. The magnetization is then given by

$$M = NgJ\mu_\mathrm{B} B_J(x) \,, \quad \text{with } x = gJ\mu_\mathrm{B}\mu_0\lambda M/k_\mathrm{B}T \,, \tag{2.5}$$

with $B_J(x)$ the Brillouin function.[14] In the case of $J = 1/2$ this equation simplifies to equation (2.4). In Fig. 2.1 the resulting magnetization is plotted as a function of temperature for a few values of J.

2.2 Ultrafast Demagnetization

2.2.1 Three Temperature Model

As mentioned in the introduction, the ultrafast demagnetization found by Beaurepaire *et al.* could be explained by assuming that the complete system can be

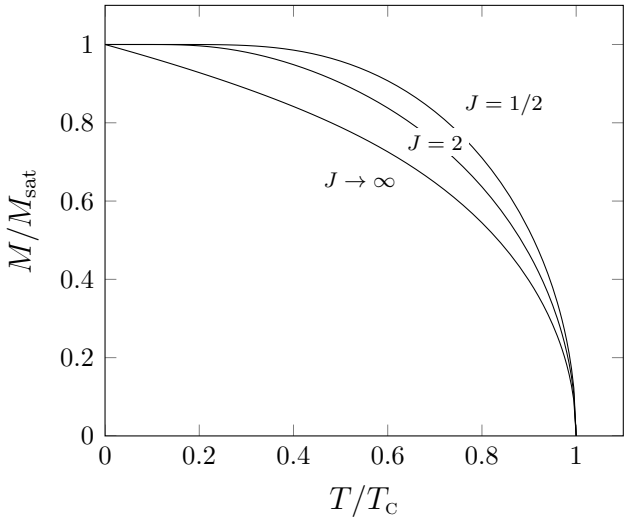

Figure 2.1: Magnetization as a function of temperature for various values of J, as given by equation (2.5).

divided into three separate subsystems, i.e. a spin, electron and phonon system. The evolution of each of the systems can then be described by three coupled differential equations:[8]

$$\begin{aligned} c_e[T_e]\frac{\mathrm{d}T_e}{\mathrm{d}t} &= -g_{ep}(T_e - T_p) - g_{es}(T_e - T_s) + P(t)\,, \\ c_s[T_s]\frac{\mathrm{d}T_s}{\mathrm{d}t} &= -g_{es}(T_s - T_e) - g_{sp}(T_s - T_p)\,, \\ c_p[T_p]\frac{\mathrm{d}T_p}{\mathrm{d}t} &= -g_{ep}(T_p - T_e) - g_{sp}(T_p - T_s)\,. \end{aligned} \tag{2.6}$$

The evolution of the temperature T_i of subsystem i thus depends on the temperature difference with system j times a coupling constant g_{ij}, and the specific heat c_i of the subsystem. The electron system includes an extra term $P(t)$, which represents absorption of the laser.

This set of equations provides a phenomenological description of the demagnetization that can accurately fit the results. However, in order to gain more predictive power, the microscopic origins of the interactions were inserted in this model by Koopmans *et al.*,[9] who then named it the microscopic three temperature model (M3TM). In the following section these interactions will be discussed briefly, and the resulting set of equations is presented.

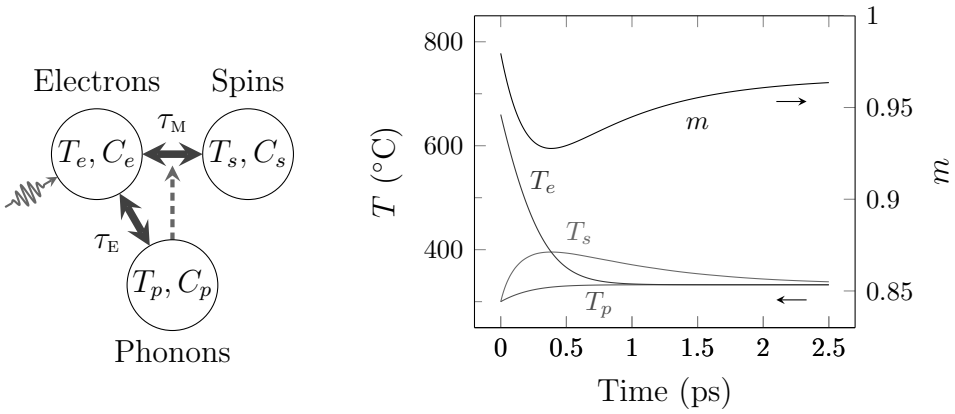

Figure 2.2: (a) The interactions allowed between the three subsystems in the M3TM model, with e–s equilibration on a timescale τ_M, and e–l equilibration on a timescale τ_E. The dashed arrow indicates transfer of angular momentum. (b) Example of a solution of the M3TM model. Here the time-evolution of the three temperatures are plotted, together with the demagnetization resulting from the change in spin temperature.

2.2.2 Microscopic Description

One of the problems of the 3TM as introduced by Beaurepaire *et al.* is that it does not take conservation of angular momentum into consideration. The fact that angular momentum plays an important role in changing the magnetization direction can be seen from the Einstein–De Haas effect, where a ferromagnetic material gains a rotational motion when its magnetization is reversed. The change in magnetization thus requires angular momentum to be transferred from the spin system.

In the M3TM model, this transfer of spin momentum is assumed to be mediated by the Elliot–Yafet mechanism. Here, the conduction band states are assumed to be a linear combination of the spin states due to spin-orbit coupling.[15] Because of this, with each electron–phonon scattering event the electron has a chance to couple to a different spin state, changing its spin orientation and transferring angular momentum into the lattice. Through this spin-flip scattering the electron and spin systems will equilibrate. Furthermore, electron–phonon scattering will cause the electron and phonon systems to equilibrate. Figure 2.2 (a) gives a schematic representation of the three systems and the allowed interactions.

Using these interactions, the temperature of each system can be calculated as a function of time. This is done by describing the spin system with a Weiss mean

field model, the phonon system with a Debye model, and the electron system as a Fermi sea of spinless particles.

First, the *e–p* equilibration is calculated. For this, the electron system is assumed to follow Fermi–Dirac statistics, with a constant density of states D_{F} around the Fermi energy. The phonons are assumed to follow an Einstein model of identical oscillators obeying Bose–Einstein statistics, where each atomic site allows for D_p harmonic oscillators with an excitation energy of E_p. Using Fermi's golden rule, the change in the phonon population due to electron–phonon scattering can be calculated after an instantaneous increase of the electron temperature T_e. This change in population can be coupled to a change in temperature, after which the following characteristic electron–phonon equilibration time is found:[16]

$$\tau_{\mathrm{E}} = \frac{\hbar\pi k_{\mathrm{B}} T_e}{6 D_{\mathrm{F}} D_p E_p \lambda_{ep}^2} \,.$$

In this equation λ_{ep} is the matrix element of e-p scattering.

Furthermore, the specific heat of the electron system can be written as

$$c_e = \frac{\pi^2 D_{\mathrm{F}} k_{\mathrm{B}}^2}{3 V_{\mathrm{at}}} T_e \,,$$

with V_{at} the atomic volume. Assuming a constant phonon specific heat, which is approximately the case above the Debye temperature, this characteristic equilibration time can also be written as $\tau_{\mathrm{E}} = c_e / g_{ep}$, which results in a coupling constant given by[17]

$$g_{ep} = \frac{2\pi D_{\mathrm{F}}^2 D_p E_p k_{\mathrm{B}}}{\hbar V_{\mathrm{at}}} \lambda_{ep}^2 \,. \tag{2.7}$$

With this coupling constant the electron–phonon equilibration can thus be described.

The next step is then to calculate the spin-flip rate. Because the spin specific heat is relatively small, the inclusion of the spin system is assumed to have a negligible effect on the electron–phonon dynamics. Using Fermi's golden rule, the rate of change of the spin population can be calculated within the Weiss model in a similar fashion, after which the magnetization can be shown to follow

$$\frac{dm}{dt} = Rm \frac{T_p}{T_{\mathrm{C}}} \left(1 - m \coth\left(\frac{m T_{\mathrm{C}}}{T_e} \right) \right) \,, \tag{2.8}$$

with $m = M/M_{\mathrm{sat}}$, and R a constant. Assuming a Debye model for the phonons, R is given by

$$R = \frac{8 a_{sf} g_{ep} k_{\mathrm{B}} T_{\mathrm{C}}^2 V_{\mathrm{at}}}{(\mu_{\mathrm{at}}/\mu_{\mathrm{B}}) E_{\mathrm{D}}^2} \,,$$

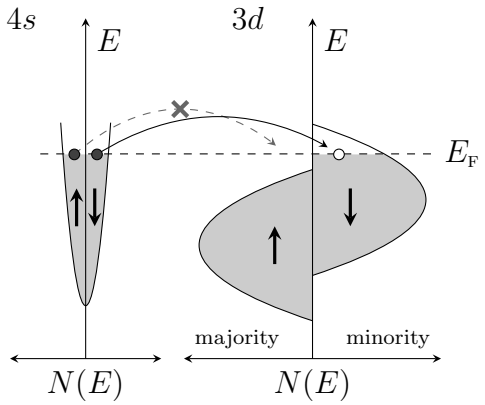

Figure 2.3: Simple representation of the density of states of 3*d*- and 4*s*-bands. Due to the availability of minority holes in the 3*d*-bands, the conductivity of *s* electrons with their spins aligned antiparallel to the magnetization will be reduced.

with a_{sf} the spin-flip probability at each electron–phonon scattering event, and E_{D} the maximum phonon energy. With these interactions all three systems can be described. Figure 2.2 (b) shows an example solution of the M3TM model, where each of the three temperatures is plotted, together with the magnetization as a function of time.

2.3 Spin-dependent Transport

2.3.1 Giant Magnetoresistance

One of the main goals of this thesis to investigate whether electron transport through a device can be controlled using a spin-valve structure. A spin-valve is a device consisting of two or more magnetic layers, in which the resistance can change depending on the alignment of the magnetization of these layers. When the layers are aligned antiparallel, the device will have a relatively high resistance, while the resistance is lowered when the layers are aligned parallel. This change in resistance is called the giant magnetoresistance (GMR) effect.

GMR can be explained using spin-dependent electron mobilities. The fact that mobilities are spin-dependent was first demonstrated by Mott,[18] who showed that ferromagnetic transition metals have a lower resistance when the electron spin is aligned with the magnetization. This can be seen by looking at the density of states around the Fermi level, which is schematically depicted in Fig. 2.3 for a

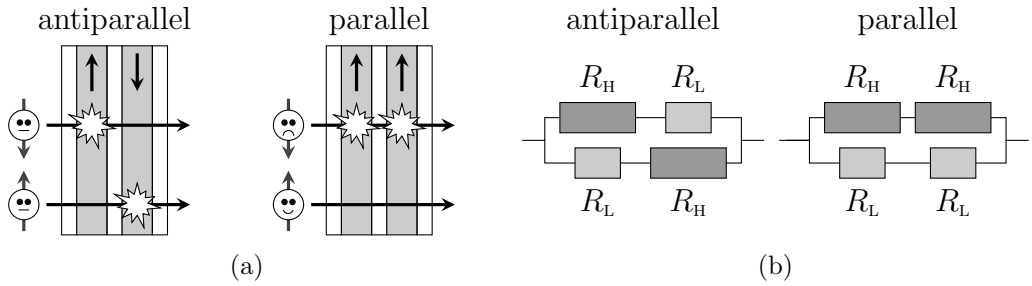

Figure 2.4: (a) A device consisting of two magnetic layers. Due to spin-dependent scattering the resistance of this device will be relatively large in the case of antiparallel alignment. However, if the layers are aligned parallel, resistance is decreased due to the presence of a conductive path. (b) Equivalent circuits for both configurations.

$3d$ transition metal. Since the $3d$-bands are strongly localized, conduction will be governed by the $4s$-electrons. However, minority $4s$-electrons will interact with holes in the $3d$-band, decreasing their mobility. This is not the case for majority electrons, which have a largely filled $3d$-band.

Inside a device containing multiple magnetic layers, this spin-dependent conductivity will result in a resistance depending on the alignment of the layers. This is shown in Fig. 2.4 (a), where two electrons with different spins move through a device consisting of two separated magnetic layers. Electrons with their spin directed opposite to the magnetization of one of these layers will undergo additional scattering. In the case of antiparallel alignment of the magnetic layers all electrons will therefore experience scattering. However, in the case of parallel alignment, one of the spin channels will form a conductive path, lowering the total resistance of the device.

Neglecting the presence of spin-flip scattering inside the device, the two spin channels can be treated as separate current paths. In this case the two circuits shown in Fig. 2.4 (b) are equivalent to the two configurations of the device.[14] Here R_H denotes the high resistance experienced by minority carriers, and R_L the low resistance for majority carriers. The resistances of these circuits are

$$\begin{aligned} R_{AP} &= \frac{R_H + R_L}{2}\,, \\ R_P &= \frac{2R_H R_L}{R_H + R_L}\,. \end{aligned} \tag{2.9}$$

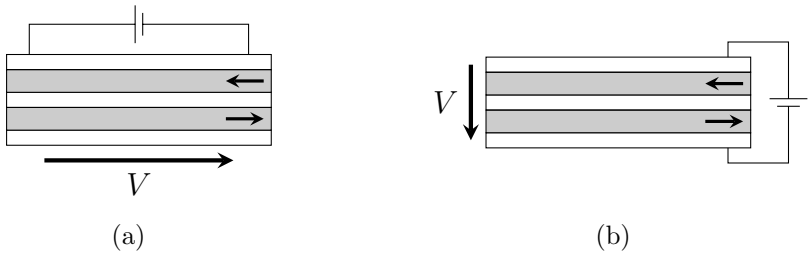

Figure 2.5: Two configurations for measuring the GMR ratio, with the current direction either (a) in plane (CIP) or (b) perpendicular to the plane (CPP).

R_{H} and R_{L} can be related to the resistance of a single layer R_0 through a dimensionless parameter β:

$$\begin{aligned} R_{\mathrm{H}} &= \frac{2R_0}{1-\beta}\,, \\ R_{\mathrm{L}} &= \frac{2R_0}{1+\beta}\,, \end{aligned} \tag{2.10}$$

with $0 < \beta < 1$. The relative increase in resistance between the parallel and antiparallel configuration can then be written as

$$\begin{aligned} \frac{\Delta R}{R_{\mathrm{P}}} &\equiv \frac{R_{\mathrm{AP}} - R_{\mathrm{P}}}{R_{\mathrm{P}}} \\ &= \frac{(R_{\mathrm{H}} - R_{\mathrm{L}})^2}{4R_{\mathrm{L}}R_{\mathrm{H}}} \\ &= \frac{\beta^2}{1-\beta^2} > 0\,, \end{aligned} \tag{2.11}$$

showing that the resistance in the parallel configuration is indeed lower.

Spin valves can be measured in two different configurations. In the current in plane (CIP) geometry, electrodes are attached to the sides of the spin valve, and current passes through the device in the direction of the plane. This is shown in Fig. 2.5 (a). In the second configuration, current passes perpendicular to the plane (CPP) of the spin valve. This gives a larger GMR effect, since in the CIP configuration conduction is mostly governed by the conducting spacer layer, while this is no longer the case in the CPP configuration. However, since electrodes now have to be placed at both the top and the bottom of the device, the CPP configuration is much more difficult to fabricate.

In the experiment proposed in section 1.3, the spin valve is used in the CPP configuration, since electrons are excited on one side, after which they travel in

the direction perpendicular to the plane. However, all measurements on the GMR effect presented in chapter 6 were done in the CIP configuration. Nevertheless, the CIP GMR ratio can be used as a good measure of the CPP ratio since in both configurations the GMR ratio depends on the spin dependent resistivities of the magnetic layers.

2.3.2 Giant Magnetothermal Resistance

Besides a change in resistance, a change in heat conduction is also expected when the alignment of the magnetic layers changes. Heat transport inside a solid material is often described by the movement of phonons and electrons. Since inside metals there is a large amount of free electrons which move much faster than phonons, the contribution of the electrons to the heat conduction is much greater. Because of this, the heat conduction is coupled to the electrical conduction. This is described by the empirical Wiedemann–Franz law, which states that

$$\frac{\kappa}{\sigma} = LT\,, \tag{2.12}$$

where κ is the heat conduction, σ the electrical conduction, and T the temperature. The constant L is called the Lorenz number.

To get an approximate value of the Lorenz number, both conductivities can be calculated using the Drude model. According to this model, the electrical conductivity of a metal can be written as

$$\sigma = \frac{ne^2\lambda}{m\bar{v}}\,,$$

with n the electron density, e the elementary charge, m the mass of an electron, λ the mean free path, and $\bar{v}$ the average speed. With the same model the heat conduction can be written as

$$\kappa = \frac{1}{3}\lambda\bar{v}C_e\,,$$

where C_e is the electronic heat capacity. With $C_e = \frac{3}{2}k_\mathrm{B}n$ and $\bar{v} = \sqrt{3k_\mathrm{B}T/m}$, this gives the following ratio between the electric and heat conductivity:

$$\frac{\kappa}{\sigma} = \frac{3k_\mathrm{B}^2}{2e^2}T\,. \tag{2.13}$$

This then gives a value of $L = 1.11 \cdot 10^{-8}\ \mathrm{V^2\,K^{-2}}$.[19] Since this is a crude description of how electrons behave inside a material, it only gives the correct order of

Table 2.1: Experimental values of the Lorenz number L. Values are taken from Ref. 19.

Metal	L (0 °C)	L (100 °C)	Metal	L (0 °C)	L (100 °C)
	(10^{-8} V^2 K^{-2})			(10^{-8} V^2 K^{-2})	
Ag	2.31	2.38	Li	2.22	2.43
Au	2.35	2.36	Mo	2.61	2.79
Al	2.14	2.19	Pb	2.47	2.53
Cu	2.23	2.29	Pt	2.51	2.60
Fe	2.61	2.88	W	3.04	3.20
Ir	2.49	2.49	Zn	2.28	2.30

magnitude for the Lorenz number. By calculating both conductivities using the Boltzmann transport equation, the Lorenz number can be shown to have a value of $L = 2.45 \cdot 10^{-8}$ V^2 K^{-2}.[20] This value is indeed in better correspondence to the experimental results, which are shown in Table 2.1.

Due to this proportionality, the heat conduction of a GMR stack is expected to change in the same way as the electrical conduction. This is called giant magnetothermal resistance (GMTR). However, as it turns out, the Lorenz number changes in different configurations, giving a difference in GMR and GMTR values.[21] In all literature found, the Lorenz number is increased in the parallel configuration, resulting in a larger GMTR effect. This is assumed to be due to inelastic scattering having a larger effect on heat conduction than electric conduction.[22,23] In the case of parallel alignment this is no problem, since the majority carriers, which dominantly contribute to the transport, undergo relatively little scattering. However, for antiparallel alignment scattering becomes more important, causing a larger decrease in heat transport.

2.4 Ultrafast Heat Transport

In this thesis the effects of transport on ultrafast laser-induced demagnetization will be investigated. However, at these extremely short length- and timescales it is still under debate which type of transport dominates. In the next section we will briefly discuss the three types of transport that can take place, which are diffusive, ballistic and superdiffusive transport.

2.4.1 Diffusive Transport

Heat transport at large timescales can best be described statistically. In this case all particles are assumed to scatter frequently, by which their path can be described as a random walk. For a large amount of particles, their displacement will follow a Gaussian distribution, where the variance increases according to $\sigma \propto \sqrt{t}$.[24]

When a temperature difference is present, diffusive transport will result in a heat flux given by

$$q = -\kappa \nabla T \,.$$

This results in a change in temperature given by

$$c\frac{dT}{dt} = -\nabla(\kappa \nabla T)\,, \tag{2.14}$$

with c the specific heat of the material. As mentioned before, heat transport in metals is governed by electrons, and heat transport by phonons can be neglected.

2.4.2 Ballistic Transport

The second type of transport is ballistic transport. When electrons are excited from below the Fermi energy, they will start to move in a straight line with a speed close to the Fermi speed v_{F} until they scatter. As long as the electron does not scatter, its displacement will increase linearly with time.

In metals, the relaxation of hot electrons is typically determined by electron–electron scattering. The characteristic timescale between two collisions is generally written as

$$\tau_{ee} = \frac{1}{K_{ee}(E - E_{\mathrm{F}})^2}\,, \tag{2.15}$$

with K_{ee} the electron–electron scattering constant. Typical values of $1/K_{ee}$ found in literature are 3–5 $\mathrm{fs\,eV^2}$ for Co, Fe and Ni, or ~ 60 $\mathrm{fs\,eV^2}$ for Cu, Au or Ag.[25,26] Furthermore, in ferromagnetic materials the lifetime of majority carriers has been found to be larger by a factor of up to 2.

2.4.3 Superdiffusive Transport

Although equation (2.15) gives a good description of the relaxation time of a single electron, the lifetime of the total electron concentration is much larger due

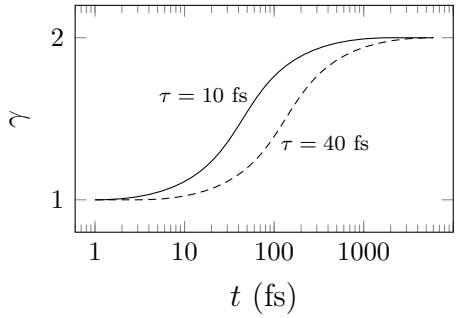

Figure 2.6: Schematic illustration of the time evolution of γ for two different characteristic scattering times, as it was calculated in Ref. 11.

to secondary electrons being excited at each collision.[27] In order to account for these second and higher order electron cascades, Battiato *et al.*[11] proposed a superdiffusive model, where on short timescales electrons move ballistically, but on longer timescales transport is governed by cascades of electrons.

The mean squared displacement of a single-particle distribution can generally be written as

$$\langle x(t)^2 \rangle \propto K t^{2/\gamma} \,, \tag{2.16}$$

with K the diffusion constant, and γ the anomalous diffusion exponent. Diffusive transport is characterized by $\gamma = 2$, ballistic transport by $\gamma = 1$. Superdiffusive transport is then transport in the regime of $1 < \gamma < 2$.

In the model used in Ref. 11 transport starts out with $\gamma = 1$, but after a short time, typically 10–100 fs depending on the mean-free-path of the electrons, transport will shift to the diffusive regime with $\gamma = 2$. Figure 2.6 shows a schematic illustration of the typical development of γ within this superdiffusive transport model.

2.5 Laser Absorption

2.5.1 Transfer Matrix Method

Since in this thesis all measurements of the demagnetization are done after heating a multilayer with a laser pulse, it is important to be able to calculate the amount of energy absorbed inside each layer. This is done using the so-called transfer matrix method. This method provides a straightforward way of calculating the electric fields at each interface, after which the electric field at any intermediate position

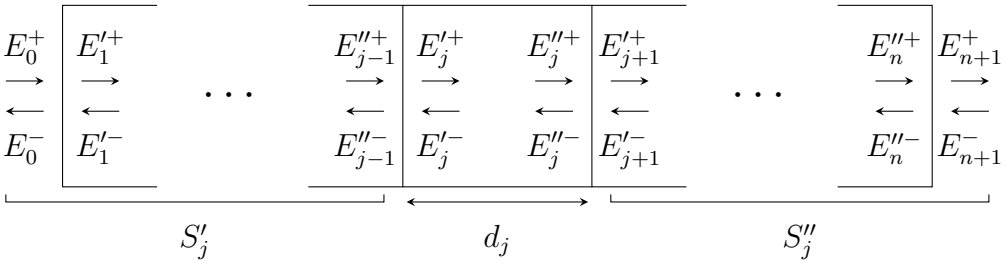

Figure 2.7: Sketch of the multilayered stack, together with the electric fields as they are defined for the derivation of equation (2.23).

can be calculated. Figure 2.7 shows the electric fields at these interfaces, together with some other variables that will be used in the following derivation.

Assuming perpendicular incident light moving through a stack of n materials, the electric field inside the j-th material can be written as the sum of a forward propagating wave and a backward propagating wave:

$$E_j(z,t) = E_j^+(z,t) + E_j^-(z,t)\,, \tag{2.17}$$

where the two waves are given by

$$E_j^\pm(z,t) = E_{j,0}^\pm e^{\left(i\left(\pm\frac{2\pi}{\lambda}\tilde{n}_j z - \omega t\right)\right)}\,, \tag{2.18}$$

with λ the wavelength and ω the angular frequency of the light. Furthermore, $\tilde{n}_j$ is the complex index of refraction, which is given by

$$\tilde{n}_j = \eta_j + i\kappa_j\,. \tag{2.19}$$

The real part η determines properties such as velocity and refraction in the usual way. The implications of the imaginary part κ_j, which is also called the extinction coefficient, will be discussed in section 2.5.2.

Using equation (2.18), the electric field at one side of the material $E_j'(t)$ can be related to the field at the other side $E_j''(t)$ through

$$\begin{aligned} E_j'^+(t) &= e^{-i\frac{2\pi}{\lambda}\tilde{n}_j d_j} E_j''^+(t)\,, \\ E_j'^-(t) &= e^{i\frac{2\pi}{\lambda}\tilde{n}_j d_j} E_j''^-(t)\,, \end{aligned} \tag{2.20}$$

with d_j the thickness of the j-th material. Furthermore, using the Fresnel coefficients of reflection r and transmission t, given by

$$\begin{aligned} r_{j-1,j} &= \frac{\tilde{n}_{j-1} - \tilde{n}_j}{\tilde{n}_{j-1} + \tilde{n}_j}\,, \\ t_{j-1,j} &= \frac{2\tilde{n}_{j-1}}{\tilde{n}_{j-1} + \tilde{n}_j}\,, \end{aligned}$$

we can relate the electric fields on both sides of the interface through

$$\begin{aligned} t_{j-1,j}E''^{+}_{j-1}(t) &= E'^{+}_{j}(t) + r_{j-1,j}E'^{-}_{j}(t)\,, \\ t_{j-1,j}E''^{-}_{j-1}(t) &= E'^{-}_{j}(t) + r_{j-1,j}E'^{+}_{j}(t)\,. \end{aligned} \tag{2.21}$$

The set of equations (2.20) and (2.21) can be rewritten into a series of matrices. Defining the interface matrix $I_{j-1,j}$ and layer matrix $L_{j-1,j}$ as[28]

$$\begin{aligned} I_{j-1,j} &= \frac{1}{t_{j-1,j}} \begin{pmatrix} 1 & r_{j-1,j} \\ r_{j-1,j} & 1 \end{pmatrix}\,, \\ L_j &= \begin{pmatrix} e^{-i\frac{2\pi}{\lambda}\tilde{n}_j d_j} & 0 \\ 0 & e^{i\frac{2\pi}{\lambda}\tilde{n}_j d_j} \end{pmatrix}\,, \end{aligned}$$

then allows the amplitude of the electric field at the interfaces to be written as

$$\begin{aligned} \begin{pmatrix} E^{+}_{0} \\ E^{-}_{0} \end{pmatrix} &= S'_j \begin{pmatrix} E'^{+}_{j} \\ E'^{-}_{j} \end{pmatrix}\,, \\ \begin{pmatrix} E'^{+}_{j} \\ E'^{-}_{j} \end{pmatrix} &= S''_j \begin{pmatrix} E^{+}_{n+1} \\ E^{-}_{n+1} \end{pmatrix}\,, \end{aligned}$$

with the transfer matrices S'_j and S''_j given by

$$\begin{aligned} S'_j &= \begin{pmatrix} S'_{j11} & S'_{j12} \\ S'_{j21} & S'_{j22} \end{pmatrix} = \left(\prod_{k=1}^{j-1} I_{k-1,k}L_k \right) \cdot I_{j-1,j}\,, \\ S''_j &= \begin{pmatrix} S''_{j11} & S''_{j12} \\ S''_{j21} & S''_{j22} \end{pmatrix} = \left(\prod_{k=j+1}^{n} I_{k-1,k}L_k \right) \cdot I_{n,n+1}\,. \end{aligned} \tag{2.22}$$

Finally, if we assume that $E^{-}_{n+1} = 0$, it can be shown that the amplitude of the electric field at any location can then be written as a function of the incident plane wave:

$$E_j(z) = \frac{S''_{j11} \cdot e^{-i\frac{2\pi}{\lambda}\tilde{n}_j(d_j - z)} + S''_{j21} \cdot e^{i\frac{2\pi}{\lambda}\tilde{n}_j(d_j - z)}}{S'_{j11}S''_{j11} \cdot e^{-i\frac{2\pi}{\lambda}\tilde{n}_j d_j} + S'_{j12}S''_{j21} \cdot e^{i\frac{2\pi}{\lambda}\tilde{n}_j d_j}} E^{+}_{0}\,. \tag{2.23}$$

2.5.2 Absorption

Now that the electric field throughout the device is known, the amount of absorption can be calculated. For light traveling through a dielectric material, the loss

of intensity depends on the extinction coefficient κ of the material. This can be seen by inserting equation (2.19) into the solution of a propagating wave:

$$E(z,t) = E_0 e^{i(\frac{2\pi}{\lambda}(\eta+i\kappa)z-\omega t)} = E_0 e^{i(\frac{2\pi}{\lambda}\eta z-\omega t)} e^{-\frac{2\pi}{\lambda}\kappa z}\,.$$

Since the intensity of an electromagnetic wave is proportional to E^2, we thus find a wave decaying exponentially with a characteristic length of $1/\alpha$, where the so-called attenuation coefficient α is given by

$$\alpha = \frac{4\pi}{\lambda}\kappa\,. \tag{2.24}$$

This decay in intensity is also known as the Beer–Lambert law.

To get a more quantitative expression for the absorption rate, the change in energy of an electromagnetic wave travelling through a dielectric material can be calculated. According to Poynting's theorem, the change in the energy density u is given by

$$\frac{\partial u}{\partial t} = -\nabla\cdot\mathbf{S} = -\nabla\cdot\left(\frac{1}{\mu_0\mu_r}\mathbf{E}\times\mathbf{B}\right)\,, \tag{2.25}$$

where $\mathbf{S}$ is called the Poynting vector. In this equation, $\mathbf{E}$ and $\mathbf{B}$ are the real parts of the complex vectors $\tilde{\mathbf{E}}$ and $\tilde{\mathbf{B}}$. The magnetic field can be expressed in terms of the electric field using the Maxwell–Faraday equation:

$$\nabla\times\mathbf{E} = -\frac{\partial\mathbf{B}}{\partial t}\,.$$

If we now assume a plane wave traveling in the z direction with its electric field polarized along the x-axis, this will yield the following general solution to the Maxwell equations:[29]

$$\begin{aligned}\tilde{\mathbf{E}}(z,t) &= \tilde{E}_0 e^{-\frac{2\pi}{\lambda}\kappa z} e^{i(\frac{2\pi}{\lambda}\kappa z-\omega t)}\,\hat{\mathbf{x}}\,,\\ \tilde{\mathbf{B}}(z,t) &= \frac{2\pi}{\lambda\omega}\tilde{n}\tilde{E}_0 e^{-\frac{2\pi}{\lambda}\kappa z} e^{i(\frac{2\pi}{\lambda}\kappa z-\omega t)}\,\hat{\mathbf{y}}\,,\end{aligned} \tag{2.26}$$

with the complex constant $\tilde{E}_0 = E_0 e^{i\delta}$ determining the initial amplitude and phase of the wave.

We thus find a magnetic field with not only a change in amplitude of $2\pi|\tilde{n}|/\lambda\omega$ as compared to the electric field, but also a shift in phase of $\phi \equiv \tan^{-1}\kappa/\eta$ due to the fact that the refractive index is a complex number. Figure 2.8 shows the real part of this solution as as a function of z.

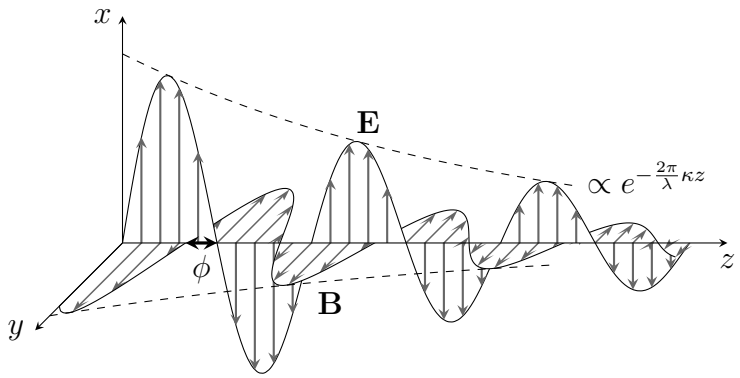

Figure 2.8: The solution of the wave equation inside a dielectric material at different positions. Because the index of refraction is now a complex number the wave will decay, and the electric and magnetic fields will shift in phase by an amount of ϕ.

We can rewrite this phase shifted term by using the fact that $a\sin(\theta) + b\cos(\theta) = \cos(\theta+\phi)$, where $\phi+\pi/2 = \sin^{-1}(b/\sqrt{a^2+b^2})$ and $\sqrt{a^2+b^2} = 1$, which in this case results in $a = \kappa/|\tilde{n}|$ and $b = \eta/|\tilde{n}|$. This then allows us to write the time-averaged length of the Poynting vector as

$$\begin{aligned}\langle S\rangle &= \frac{1}{\mu_0\mu_r}\frac{2\pi}{\lambda\omega}|\tilde{n}||\mathbf{E}|^2 \cdot \left\langle \cos\left(\frac{2\pi}{\lambda}\kappa z - \omega t + \delta\right)\cdot\cos\left(\frac{2\pi}{\lambda}\kappa z - \omega t + \delta + \phi\right)\right\rangle \\ &= \frac{1}{\mu_0\mu_r}\frac{2\pi}{\lambda\omega}|\mathbf{E}|^2 \cdot \frac{1}{2}\eta\,. \end{aligned} \tag{2.27}$$

Combining equations (2.25) and (2.27), we find the time-averaged change in energy density:

$$Q \equiv \left\langle \frac{\partial u}{\partial t}\right\rangle = \langle -\nabla\cdot\mathbf{S}\rangle = -\frac{\mathrm{d}}{\mathrm{d}z}\langle S\rangle = \frac{1}{2}c\epsilon_0\alpha\eta|E(z)|^2\,, \tag{2.28}$$

where we have used $2\pi/\lambda\omega = 1/c = \mu_0\epsilon_0 c$, and assumed that $\mu_r \approx 1$. This expression indeed corresponds to the one used in Ref. 28.

Chapter 3

Methods

All demagnetization measurements done in this thesis were done using a TR-MOKE setup. How this setup works will be explained in this chapter. First, the regular MOKE setup is presented. After this, the TR-MOKE setup is presented, and a few important elements of this setup are discussed.

3.1 Magneto-Optical Kerr Effect

When light is reflected off a magnetic material, it will undergo a change in polarization. This is called the magneto-optical Kerr effect (MOKE). It is similar to the Faraday effect, where the polarization of the light changes when being transmitted through a magnetic medium.

Microscopically, both effects arise due to a combination of the optical selection rules and spin-orbit coupling, but they are easily explained phenomenologically. Due to the magnetization, left-handed and right-handed circularly polarized light will both (1) travel through the medium at different speeds, and (2) undergo different absorption rates. Since linearly polarized light can be seen as a superposition of left- and right-handed polarized light, it will undergo a rotation due to effect (1), and gain an ellipticity due to effect (2). This is schematically pictured in Fig. 3.1.

In order to measure MOKE signal with an improved signal-to-noise ratio, the signal can be filtered out by placing a photo-elastic modulator (PEM) in the path of the probe beam. A PEM consists of a birefringent crystal whose birefringence depends on the applied stress. By alternating the stress at the crystal's resonant frequency — in our case 50 kHz — large amplitudes of birefringence can be achieved.

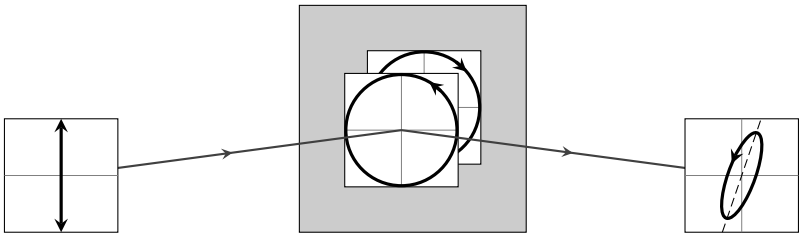

Figure 3.1: Linearly polarized light reflecting off a magnetic material will gain both a Kerr rotation and ellipticity. This is due to the magnetic material having a different refractive index for left- and right-handed circularly polarized light.

A PEM will thus give a time–dependent retardation in one direction of $A\cos(\Omega t)$, with Ω the PEM's frequency, and A the maximum retardation. Using the Jones formalism the PEM can be represented by the matrix

$$M_{\text{PEM}} = \begin{bmatrix} 1 & 0 \\ 0 & e^{iA\cos(\Omega t)} \end{bmatrix} . \tag{3.1}$$

With A set to $\frac{1}{2}\pi$ a linearly polarized beam hitting the PEM under 45°, i.e. $\frac{1}{\sqrt{2}}\binom{1}{1}$, will be modulated between left- and right-handed circular polarization, i.e. $\frac{1}{\sqrt{2}}\binom{1}{\pm i}$.

If the modulated light is now reflected off a magnetic sample and guided to a polarizer at an angle of 0° with the PEM, it can now be shown that the intensity is given by[30]

$$V = V_{\text{static}} + V_{1f} + V_{2f} \,, \tag{3.2}$$

with V_{static} a constant value, and V_{1f} and V_{2f} given by

$$\begin{aligned} V_{1f} &= V_0 4 J_1(A)\psi_e \cos(\Omega t) \,, \\ V_{2f} &= V_0 4 J_2(A)\psi_r \cos(2\Omega t) \,, \end{aligned} \tag{3.3}$$

with V_0 a constant, J_n the n-th order Bessel function, ϕ_e and ϕ_r the angles of ellipticity and rotation respectively, and Ω the PEM frequency. By using a lock-in amplifier to filter out the part of the signal with the frequency of the PEM the Kerr ellipticity can now be accurately measured, and the Kerr rotation at twice the PEM frequency. The optimum retardation is then at the maximum of J_1 or J_2, which are 1.84 and 3.05 respectively.

Figure 3.2 shows the polarization of the probe beam as a function of time due to the PEM, together with those resulting from a Kerr rotation and a Kerr ellipticity, showing that these indeed induce an oscillation in the intensity at twice and once the PEM frequency respectively.

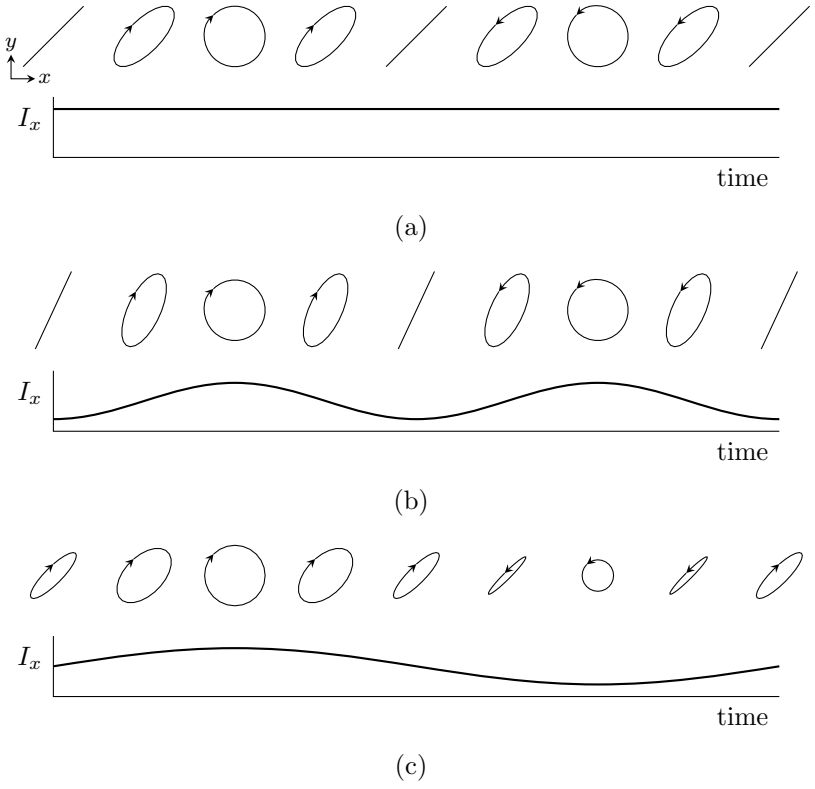

Figure 3.2: Schematic illustration of the probe beam polarization and intensity along the x–axis at a few times during one PEM period (a) for linearly polarized light, (b) for light with a Kerr rotation, and (c) for light with a Kerr ellipticity.

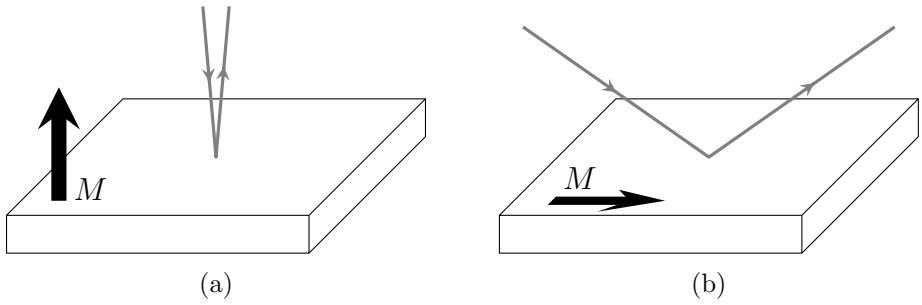

Figure 3.3: (a) Polar and (b) longitudinal configuration to increase the sensitivity to the OOP or IP magnetization respectively.

In order to gain more sensitivity for either the in-plane or out-of-plane, the angle of incidence of the laser can be altered. In this thesis the MOKE signal will either be used in the polar or the longitudinal configuration, to gain more sensitivity to the out-of-plane and in-plane magnetization respectively. With polar MOKE, the light reaches the sample close to normal incidence. With longitudinal MOKE, the light reaches the sample under an angle of roughly 60°. Both configurations are shown in Fig. 3.3.

3.2 Time-Resolved MOKE

In this thesis the effects of heating a ferromagnetic material with an ultrashort laser pulse are investigated. This is done using a pump–probe setup, where the material is excited by a pump beam, after which a probe beam is used to measure the magnetization. By changing the optical path of one of the beams, the probe pulse can be given a time delay compared to the pump pulse, allowing the magnetization to be measured at a certain time after pump excitation. This setup is called the time-resolved MOKE (TR-MOKE) setup, and is depicted in Fig. 3.4.

In this setup, laser pulses are generated using a Ti:Sapphire laser with a frequency of ~ 80 MHz. The laser pulses have a FWHM of approximately 70 fs, a wavelength of 790 nm and a maximum power of 800 mW. Once the pump beam reaches the sample, there is typically 80 mW left.

The laser pulse is first split up into an intense pump and a less intense probe beam using a beam splitter B. The intensity of the pump beam is approximately 20 times larger than the probe beam. Both beams are then directed into a delay line. Each delay line consist of a retroreflector mounted on a translation stage. By

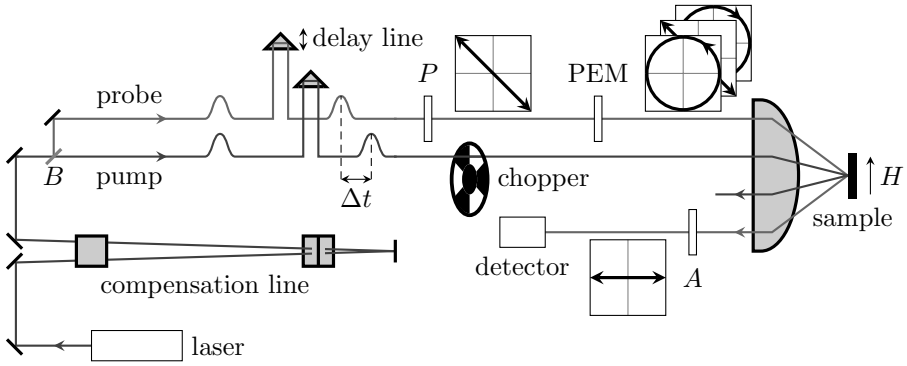

Figure 3.4: TR-MOKE setup. Two pulses with a small delay Δt are focussed on the sample. Using a PEM and polarizers P and A the magnetization can be measured. By modulating the probe beam with a chopper, noise can be further reduced using a lock-in amplifier, yielding only the pump-induced signal.

moving these retroreflectors the path length of each beam can be altered, changing the time at which they reach the sample.

The probe beam is modulated using a polarizer P and a PEM, as explained in the previous section. It is then focussed at the same spot as the pump, after which the magnetization can be measured using a second polarizer A and a light detector. The pump beam can be directed through a chopper before heating the sample, and the laser pulses can also be guided through a compensation line. These two elements will be explained in the next two sections.

Just as with the regular MOKE setup, the out-of-plane magnetization can be measured using the polar configuration, and the in-plane magnetization using the longitudinal configuration. Furthermore, the pump beam can also be guided around the sample to heat from the back, which will be referred to as the backpump setup.

3.2.1 Compensation Line

When light travels through a medium, its speed will depend on the wavelength of the light. This effect is called group velocity dispersion (GVD). Most materials have a positive GVD at the wavelength of the laser, causing red light to go faster then blue light.

If the laser light has a well defined frequency, this would not cause a problem. However, due to the extremely short duration of these pulses, the frequency becomes less well defined. In this so-called Fourier-transform limit, the product of the spread in duration and the spread in frequency has a minimum value. Ultrashort pulses therefore gain a bandwidth of frequencies, and are thus affected by

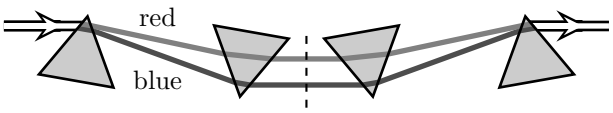

Figure 3.5: Workings of the compensation line, which adds a chirp to the laser pulse. The dashed line shows the position of the mirror.

GVD.[31] This causes the 'red' part of the pulse spectrum to arrive before the 'blue' part, lengthening the pulse duration, which is undesirable. This broadening of the pulse duration is called chirp.

The lengthening of the pulse can be counteracted by inserting a GVD compensation line in the laser path. The compensation line consists of two prisms followed by a mirror. The prisms are arranged in such a way that blue light, which is refracted at a larger angle, follows a longer path, but through less of the second prism,[32] as shown in Fig. 3.5. By changing the distance between the prisms or the position of the first prism, these two effects can be balanced to give the compensation line the opposite amount of GVD as the rest of the setup.

3.2.2 Double Modulation

As explained in section 3.1, the magnetization can be measured using a PEM to modulate the signal, and locking in at the PEM's frequency. However, this method still has a relatively low signal-to-noise ratio. In order to improve this ratio, a second modulation is added to the signal, which is again filtered out with a second lock-in amplifier. The second modulation can be added either by placing a chopper wheel in the pump path, or by oscillating the magnetic field. Figure 3.6 shows how these methods work.

Figure 3.6 (a) shows two typical field dependent measurements before and after the pump pulse has reached the sample, consisting of both the hysteresis loop of the sample plus a part linearly dependent on the magnetic field, caused by other effects such as for example Faraday rotation of the probe beam. Figure 3.6 (b) shows the resulting time-resolved signal as measured by the first lock-in.

In the case of a chopper modulation, the pump pulse will be alternately blocked and unblocked at a frequency of typically ~ 60 Hz by the chopper wheel. This will cause the signal of the first lock-in to oscillate between the value of the magnetization with and without a pump pulse reaching the sample, as is shown in Fig. 3.6 (c). Non-magnetic changes in the signal, such as the increase in reflectivity due to the increase in temperature, can be removed by subtracting the signal at a positive and a negative magnetic field and shifting the part at negative delay to zero.

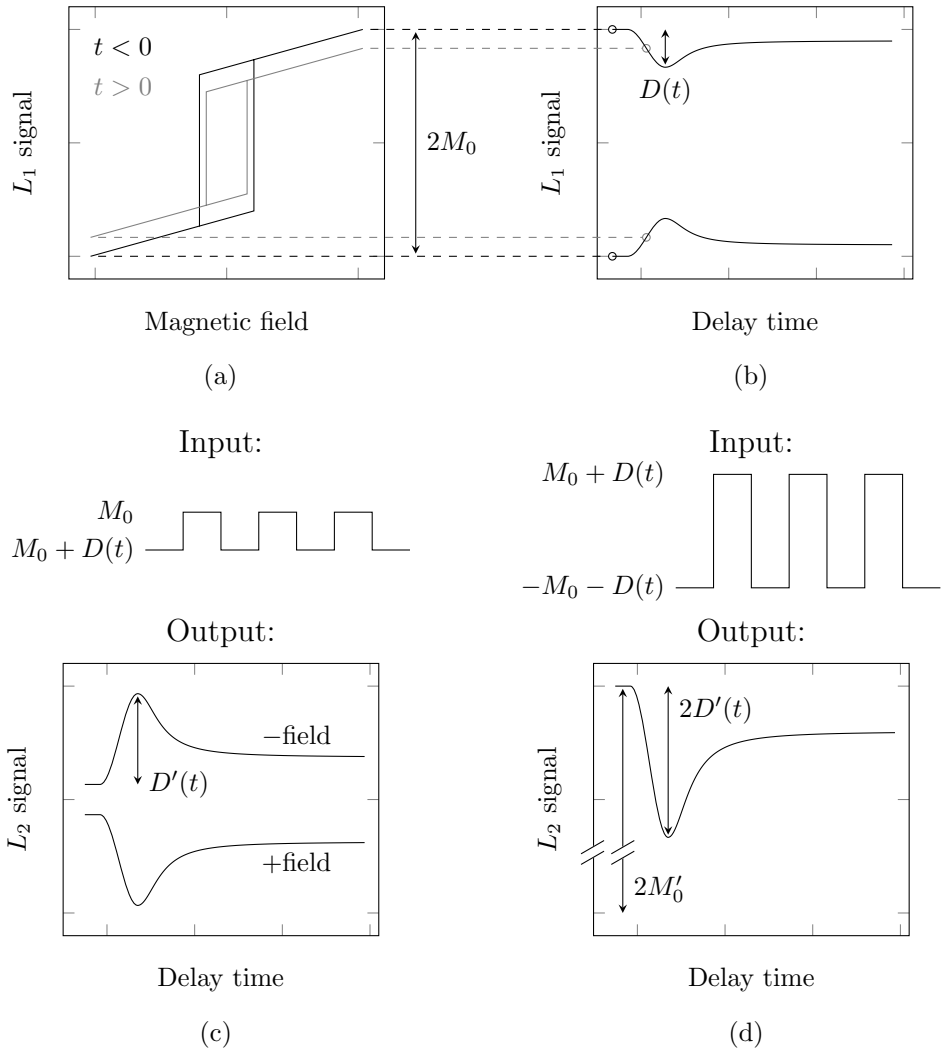

Figure 3.6: (a) Field and (b) time dependent measurements using the first lock-in, (c) second lock-in input and output using the chopper modulation, and (d) field modulation techniques. M_0 contains both the saturation magnetization and the field dependent offset caused by Faraday rotation.

Since this chopper-induced oscillation is expected to be a square wave, its $1f$ component is given by

$$\frac{2}{T}\int_0^T x(t)\sin\frac{2\pi}{T}t\,\mathrm{d}t = \frac{2}{\pi}A\,,$$

with $x(t)$ the square wave, T its period, and A its amplitude. Furthermore, a lock-in amplifier transposes its output to a scale of minus to plus 10, and as a general rule measures in RMS values,[33] allowing the demagnetization measured in the second lock-in $D'(t)$ to be related to the demagnetization in the first lock-in $D(t)$ through

$$D'(t) = \frac{10}{\sqrt{2}\cdot S_{L_2}}\frac{2}{\pi}D(t)\,,$$

with S_{L2} the sensitivity of the second lock-in. The demagnetization as compared to the saturation magnetization measured with the first lock-in can then be expressed as

$$\frac{D(t)}{M_{\mathrm{sat}}} = \frac{\pi S_{L_2}\left(D'^{+}(t) - D'^{-}(t)\right)}{10\cdot\sqrt{2}\cdot 2M_{\mathrm{sat}}}\,, \tag{3.4}$$

where $D'^{+}(t)$ and $D'^{-}(t)$ are the signals measured at a positive and a negative field respectively.

The second modulation technique used is to apply an alternating magnetic field, which is done at a frequency of ~ 2 Hz in our setup. In this case the resulting signal at a certain delay time consists of twice the total magnetization, together with an offset due to Faraday rotation, as shown in Fig. 3.6 (d). Measuring at all delay times and removing the offset would immediately yield the relative change in magnetization. However, since the field is now controlled by a function generator, this offset is difficult to determine accurately. Therefore the signal is again shifted to zero for $t < 0$, and the same factor as in equation (3.4) is used to calculate the relative demagnetization.

Both methods have a comparable amount of noise. However, the advantage of the field modulation technique is that by adjusting the field, contributions of different layers can be filtered out if they have different switching fields. Therefore, this technique is used for the final measurements in section 6.2.1.

Chapter 4

Investigating Spin Transport

Ever since the discovery of ultrafast laser-induced demagnetization it has been believed that the change in magnetization is caused by heating of the magnetic layer, after which spin angular momentum is locally transferred to other systems. However, recently a new model has been proposed by Battiato *et al.*[11] which explains the demagnetization through superdiffusive transport of non-equilibrium electrons. In this chapter two experiments are presented to differentiate between these two models. The first experiment is to investigate a nickel thin film placed on an insulating substrate after heating from both the front and the back. For the second experiment, the demagnetization of nickel placed on a conducting layer is investigated. Both these substrates are expected to have an influence on superdiffusive transport, allowing the presence of spin transport to be investigated. All experiments shown in this chapter were done using the chopper modulation scheme as explained in section 3.2.2. Both experiments display no sign of spin transport, showing that it is not the dominant process in these materials.*

4.1 Insulating Substrate

For the first experiment the demagnetization dynamics of a nickel thin film grown on top of a sapphire substrate is investigated. The nickel thin film is grown on top of the substrate using DC magnetron sputtering. Using a masking technique, the film is wedged from 0 to 30 nm over a distance of 8 mm, allowing the measurements to be done for different nickel thicknesses. Since the length of the nickel wedge

*Results shown in this chapter have been published as: A.J. Schellekens, W. Verhoeven, T.N. Vader, and B. Koopmans. "Investigating the contribution of superdiffusive transport to ultrafast demagnetization of ferromagnetic thin films," *Appl. Phys. Lett.* **102**, 252408 (2013).[34]

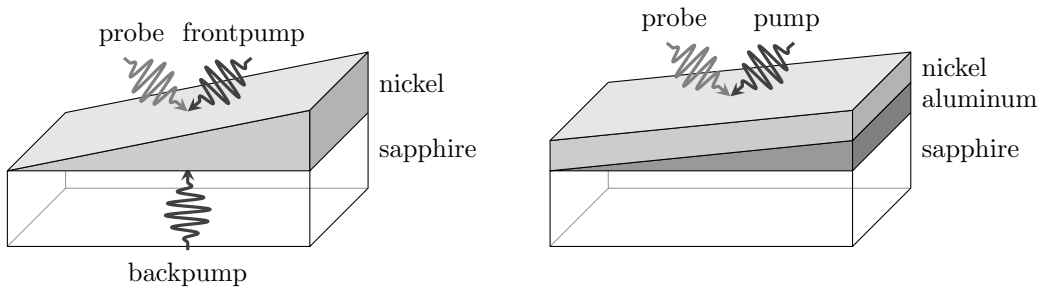

Figure 4.1: Schematic illustration of the two samples used in this chapter, consisting of (a) a Ni wedge placed on a sapphire substrate, and (b) a Ni thin film placed on an Al wedge. The Ni wedge will be measured both with a pump pulse heating from the front (frontpump setup) and from the back (backpump setup).

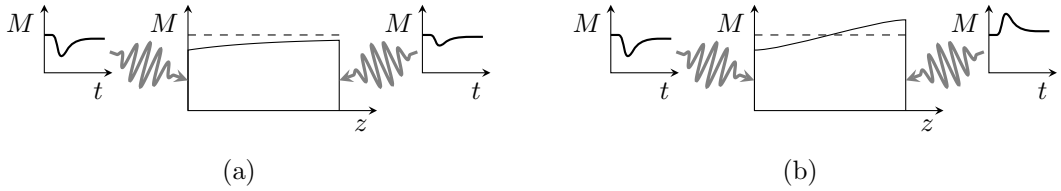

Figure 4.2: Expected spatial profile of the magnetization at a certain time after heating due to the pump pulse, and the temporal profiles measured at both sides for a demagnetization due to either (a) heating or (b) spin transport.

is much larger than the typical laser spot size of ~ 10 µm, there is no significant thickness variation over the measured area. Measurements are done both with the pump beam reaching the sample from the same side as the probe beam, which we will refer to as the frontpump setup, or from the opposite side, i.e. the backpump setup. This is shown in Fig. 4.1 (a) together with the sample layout.

If demagnetization is governed by heating of the spin system, both setups are expected to show a demagnetization. However, since sapphire is an insulating material, the superdiffusive transport model predicts that the electrons excited by the pump will move through the device and pile up at the other side. When pumping and probing from different sides the magnetization is then expected to increase.[11] This is schematically depicted in Fig. 4.2. This experiment thus offers a clear distinction between the two models.

Figure 4.3 shows the demagnetization traces for both the frontpump and the backpump measurements. This immediately shows that the magnetization decreases throughout the entire device, and that demagnetization is mainly caused by spin

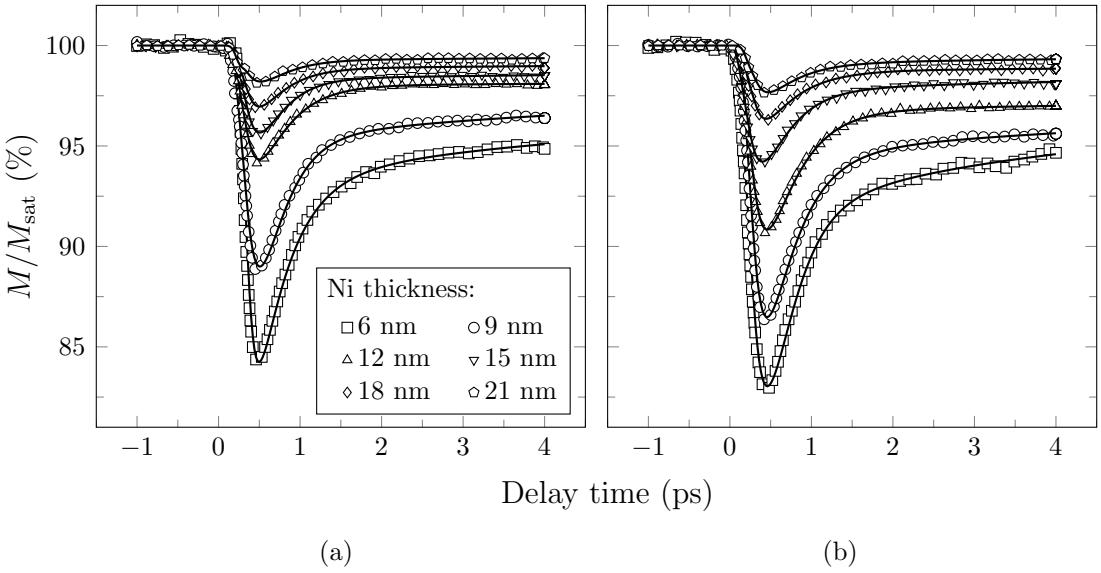

Figure 4.3: Demagnetization traces for (a) frontpump and (b) backpump setup at different Ni thicknesses.

flips, and not spin transport. We therefore conclude that even though superdiffusive transport of electrons is likely to be present in the device, it is not the main driving mechanism for demagnetization.

Phenomenologically, the demagnetization traces can be described as[16]

$$-\frac{\Delta M_z(t)}{M_{0,z}} = \Bigg[\Bigg(A_1 F(\tau_0,t) - \frac{(A_2\tau_{\mathrm{E}} - A_1\tau_{\mathrm{M}})e^{-t/\tau_{\mathrm{M}}}}{\tau_{\mathrm{E}} - \tau_{\mathrm{M}}} - \frac{\tau_{\mathrm{E}}(A_1 - A_2)e^{-t/\tau_{\mathrm{E}}}}{\tau_{\mathrm{E}} - \tau_{\mathrm{M}}}\Bigg)\Theta(t) + A_3\delta(t)\Bigg] * \Gamma(t)\,, \tag{4.1}$$

with τ_{E} the characteristic timescale of electron–phonon equilibration, and τ_{M} the timescale of magnetization loss, which incorporates both electron- and phonon-induced effects, so that no assumptions about microscopic effects have to be made. Constant A_1 represents the value after equilibrium has been restored, A_2 the initial rise in electron temperature, and A_3 effects due to temporal pump–probe overlap, such as state-filling, which can be described by the Dirac delta function $\delta(t)$. Finally, $F(\tau_0,t)$ is a function describing heat diffusion, which is chosen to be $F(\tau_0,t) = (\sqrt{t/\tau_0 + 1})^{-1}$, $\Theta(t)$ is the Heaviside step function to denote the start of heating due to the pump, and the result is convolved with a Gaussian $\Gamma(t)$ to represent the finite duration of the laser pulses. Equation (4.1) is used to fit the data in Fig. 4.3. The fitted curves are shown with the solid lines.

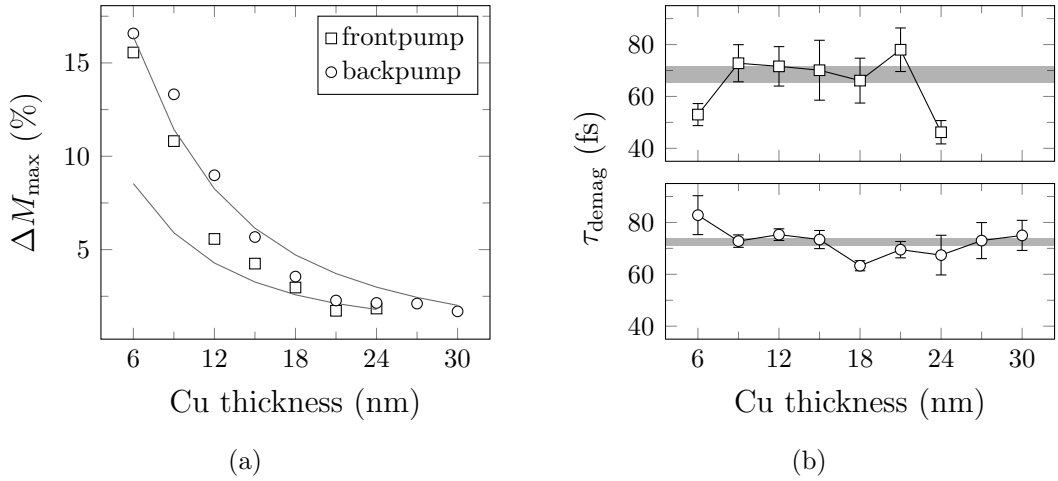

Figure 4.4: (a) Maximum demagnetization for both the front- and backpump setup. Solid lines show predictions by simulations. (b) Delay time at which the demagnetization reaches $(1 - 1/e)$ times its maximum value after deconvolving with the Gaussian pulse. Shaded areas indicate the average value with its uncertainty.

Two important features of the dependence on the nickel thickness are shown in Fig. 4.4. Figure 4.4 (a) shows the total demagnetization for both the front- and the backpump measurements, together with the values predicted by simulations. These simulated values are acquired by calculating the absorption profile with the transfer matrix method explained in section 2.5, and using this as an input for the M3TM model, which is then solved in a similar fashion as will be explained in chapter 5. This shows that the measured demagnetization traces follow approximately the same behavior. The larger demagnetization in thinner layers is mainly due to larger absorption of the laser per volume of nickel, since reflected light retains a larger intensity, resulting in a larger electric field throughout the layer. Some points deviate from the predicted values, and the difference between front- and backpump is smaller than expected, but this is attributed to the overlap of the pump and probe beams changing between subsequent measurements.

Figure 4.4 (b) shows the characteristic timescale of demagnetization. These values are obtained by deconvolving the fitted curves, and taking the time at which the demagnetization has reached $(1 - 1/e)$ times its maximum value. For both setups they remain approximately the same. Averaging these values yields demagnetization times of 69 ± 3 fs for the frontpump and 73 ± 2 fs for the backpump setup.

Both the demagnetization in the front- and backpump setup thus show a demagnetization, and amplitudes behave as expected based on a model of heating of the material. Furthermore, the characteristic demagnetization time shows no significant deviations. All measurements therefore show no sign of spin transport.

4.2 Conducting Layer

For the second experiment, a nickel layer of 10 nm was placed on top of an aluminum wedge, as shown in Fig. 4.1 (b). Due to the presence of the conducting aluminum, spin transport is expected to be enhanced. Therefore the superdiffusive transport model predicts an increased demagnetization, while no large difference is expected in a model based on local quenching of the magnetization. A few of the resulting demagnetization curves for different aluminum thicknesses are shown in Fig. 4.5. Noticeably, the demagnetization at 0 and 1 nm is smaller than at 2 and 3 nm. This smaller demagnetization is attributed to the growth of nickel being different on aluminum than on sapphire.

Figure 4.6 (a) shows the maximum demagnetization for all measured thicknesses. The solid line again denotes the values predicted by simulations. Again, the decrease in demagnetization can be explained by a smaller amount of absorbed light, and no large deviation from the expectations is found. Figure 4.6 (b) shows the characteristic demagnetization times extracted by fitting the data. Demagnetization times again remain equal within the uncertainty. Taking the average yields a demagnetization time of 73 ± 2 fs.

To conclude, no signs have been found of spin transport having an influence on the demagnetization. However, all important features show relatively large deviations between subsequent measurements, and the presence of spin transport can not be excluded, but the measurements do show that transport is not likely to be the dominant effect in nickel thin films.

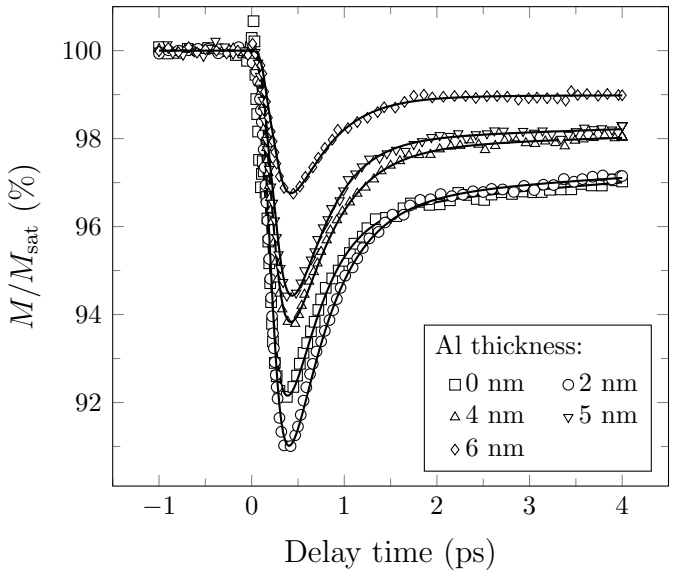

Figure 4.5: Demagnetization traces for a 10 nm Ni layer deposited on top of an Al layer for several thicknesses in the frontpump setup. Solid lines show fitted curves using equation (4.1).

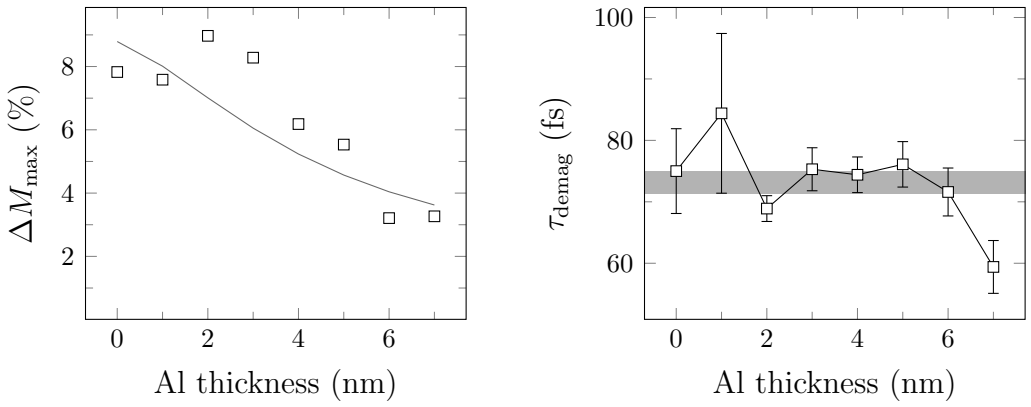

Figure 4.6: (a) Maximum demagnetization versus aluminum thickness together with the expectation from simulations, and (b) characteristic demagnetization times τ_{demag}, which are acquired in a similar fashion as in Fig. 4.4. The shaded area indicates the average and its uncertainty.

Chapter 5

Simulations on the GMTR Effect

In this chapter the results of the simulations on the GMTR effect are presented. The goal of these simulations is to get an estimation of what to expect from the experiment introduced in section 1.3, and to find the optimum device layout. This is done by solving the M3TM equations which were introduced in section 2.2.2. The implementation of this model is presented first. Then the results for a certain GMR stack, which we will refer to as the exchange biased stack, are shown for three types of transport, i.e. transport in the diffusive, ballistic and superdiffusive regimes. Finally, at the end of this chapter some simulations on a different type of GMR stack, namely a multilayered stack, are also presented, although this configuration will not be used in the measurements.

5.1 Implementation of the M3TM

As introduced in section 2.2.2, the demagnetization can be described by the following set of coupled differential equations:

$$\begin{aligned} c_e[T_e]\frac{\mathrm{d}T_e}{\mathrm{d}t} &= g_{ep}(T_p - T_e) + P(t)\,, \\ c_p\frac{\mathrm{d}T_p}{\mathrm{d}t} &= g_{ep}(T_e - T_p)\,, \\ \frac{\mathrm{d}m}{\mathrm{d}t} &= Rm\frac{T_p}{T_\mathrm{C}}\left(1 - m\coth\left(\frac{mT_\mathrm{C}}{T_e}\right)\right)\,, \end{aligned} \tag{5.1}$$

with $P(t)$ a term representing heating due to the laser pulse. If we now approximate the electronic specific heat as $c_e[T_e] = \gamma T_e$ these equations can be solved. This then

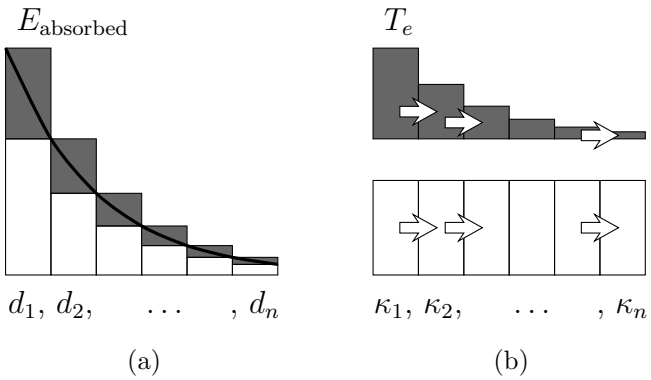

Figure 5.1: One dimensional discretization of the device in n slabs. (a) Absorbed energy is calculated for each slab separately, and is then inserted into the electron system. (b) Demagnetization dynamics can then be calculated in each slab, taking into account transport between the slabs.

yields the demagnetization of a uniform material which has been homogeneously heated.

However, for better agreement with experiments a non-uniform model is implemented. This is done by discretizing the device into n slabs, as shown in Fig. 5.1. For our purpose only a one dimensional discretization is needed, since the typical laser spot size is much larger than the device thickness, but the discretization can be extended to three dimensions if necessary.

By calculating the absorption profile as a function of depth using the transfer matrix method described in section 2.5, a slab dependent absorption can be inserted into the model. Equations (5.1) can then be solved for each slab separately. If heat transport is added between adjacent slabs, this results in a set of $3n$ coupled differential equations. Heat transport into the substrate can also be taken into account, but for our simulations this is assumed to be negligible.

Furthermore, the finite duration of the laser pulses is taken into account. The pump pulse width is included through the time-dependency of the power term in (5.1). The probe pulse width is included by applying a convolution to the results with a Gaussian pulse with respect to time. Both pulses are assumed to have a FWHM of 70 fs. For a more detailed description of both the discretization and the finite pulses the reader is referred to Ref. 35.

Finally, the probe pulse is given a position dependence. Since the Kerr effect is proportional to the electric field, it scales as $\propto e^{-\frac{2\pi}{\lambda}\kappa z}$ for thin films. However, since the reflected light has to travel back through the material, the electric field is further attenuated. The measured Kerr effect then scales as $\propto e^{-\frac{4\pi}{\lambda}\kappa z}$. Since

the absorption depends on the electric field squared, it also decreases as $\propto e^{-\frac{4\pi}{\lambda}\kappa z}$, and for thin films the two thus scale the same way.[36] It is then assumed that the same holds for multilayered stacks. The demagnetization of all slabs is therefore averaged using the absorption as a weighing factor. The final output is then the magnetization as measured by the probe pulse.

Three types of heat transport through the device will now be investigated. For diffusive transport, the temperature of a slab is altered depending on the temperature of the adjacent slabs. For ballistic and superdiffusive transport, the laser excites electrons which move through the device before depositing their energy to the rest of the system. The heating term by the laser is therefore replaced by a heating term caused by these excited electrons.

5.2 Diffusive Transport

The first system investigated is the so-called exchange biased stack, where the GMR stack consists of two separated cobalt layers, of which one is pinned due to its interaction with an antiferromagnetic material, allowing the alignment to be altered using a magnetic field. Transport between the electrons is first assumed to be diffusive. Diffusive transport is described by the equation

$$c_e[T_e]\frac{\mathrm{d}T_e}{\mathrm{d}t} = \nabla_z(\kappa\nabla_z T_e)\,, \tag{5.2}$$

with $c_e[T_e]$ the electronic specific heat, and κ the heat conduction.

In all of the simulations shown here the device consists of a layer with a perpendicular magnetic anisotropy (PMA) placed on top of a GMR stack. The PMA layer is used because in-plane cobalt shows no measurable demagnetization due to its relatively high Curie temperature. Therefore only demagnetization in this top layer is of interest, which consists of Pt (2 nm) / Co (0.5 nm) / Pt (2 nm). The GMR stack consists of Co (3 nm) / Cu (2.3 nm) / Co (3 nm) / IrMn (7 nm) (listed from top to bottom). These thicknesses are comparable to those of the stacks used in the experiments. Figure 5.2 shows this device layout. For iridium manganese the same properties as platinum were used in the simulations since not all required properties could be found, but this is not expected to be a problem since the role of the iridium manganese is small in the simulations. For the substrate sapphire was used.

The goal of these simulations is to find the optimum structure to measure the influence of the GMTR effect on the demagnetization. The effect is expected to be maximized when the temperature difference over the GMR stack is as large as

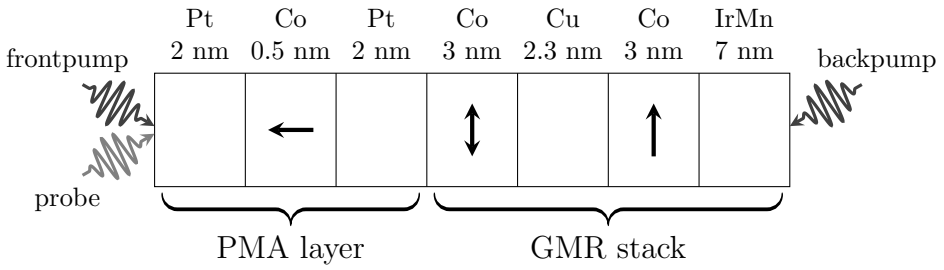

Figure 5.2: Device layout used in the simulations. The device is heated either from the front or from the back, which are referred to as the front- and backpump setups respectively.

possible, so that the flow of heat through the stack is large. This can be achieved by adding a layer with a large light absorbtion in front of the GMR stack to act as a heat supply, or a layer with little absorption to the back of the stack to act as a heat sink. However, as it turns out, adding a heat supply only increases the temperature slightly, while the extra material hinders transport considerably, resulting in a diminished effect. Therefore only the addition of a heat sink will be presented here. For the heat sink copper is used due to its small absorbtion of near-infrared light (790 nm). This causes the temperature in the copper layer to be lower despite its relatively low specific heat.

In order to add the GMTR effect to the simulations, the heat conduction of the magnetic layers is altered to differentiate between parallel and antiparallel alignment. For the simulations shown in this section the value of the heat conduction is doubled for the in-plane cobalt layers. This is a large increase, since the GMTR in these devices is expected to be smaller than 100 %, but this does give results comparable to the simulations where transport is governed by ballistic electrons. Furthermore, this is too crude a model to make quantitative predictions, and qualitative predictions are expected to depend little on the exact value.

Figure 5.3 shows the resulting time traces for antiparallel and parallel configurations. These were simulated both with the pump pulse heating from the front, i.e. the frontpump setup, or from the back, i.e. the backpump setup. This shows that we can indeed expect a small difference between the two different alignments of the GMR stack. Furthermore, whether the demagnetization increases or decreases depends on the setup. This is to be expected, since in the frontpump setup a parallel alignment causes more heat to flow away from the top layer, resulting in a smaller demagnetization. However, in the backpump setup more heat flows into the top layer in the case of a parallel alignment, resulting in a larger demagnetization. In both cases, demagnetization times remain similar for both configurations of the GMR stack.

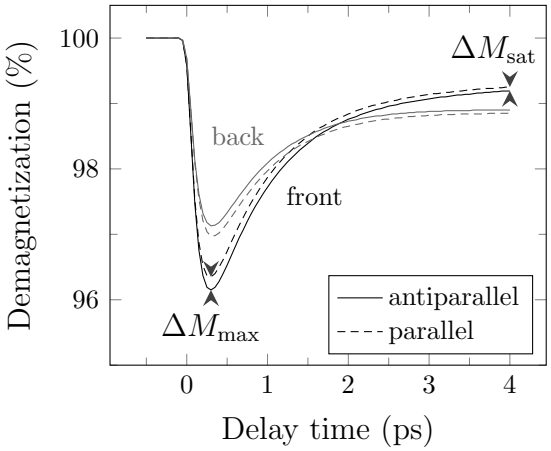

Figure 5.3: Demagnetization traces for both the frontpump and backpump setup. Arrow points denote the positions of ΔM_{max} and ΔM_{sat}, as they will be used in Fig. 5.4 and 5.5.

The next step is to find the optimum heat sink thickness, i.e. the thickness where the largest difference between the two alignments of the GMR stack can be measured. The difference is expected to be either at the maximum demagnetization in the case of relatively fast transport, or in the saturation value for relatively slow transport. These two points are shown in Fig. 5.3, and denoted by ΔM_{max} and ΔM_{sat} respectively.

For the frontpump setup, the results are shown in Fig. 5.4. Figure 5.4 (a) shows the absorption profile for both a device with and without a copper heat sink. As can be seen from this graph, the copper indeed absorbs little light, creating a large temperature difference between the heat sink and the top layer. Furthermore, it also decreases the absorption at increasing distance from the surface. This is likely due to the copper being less reflective than sapphire. The heat sink thus gives the desired temperature difference over the GMR stack.

The resulting difference in demagnetization of the top layer is shown in Fig. 5.4 (b). Shown here is the change in both the maximum and the saturation demagnetization in percentage points (ppt) when the GMR stack is switched from antiparallel to parallel alignment, which is negative. For the addition of a copper heat sink, the effect increases with increasing copper thickness, but slowly saturates, making the increase in the effect negligible after 40–50 nm. The increase in demagnetization is largest in the maximum demagnetization, making this the most promising point to measure the difference.

When the device is heated from the back the results change slightly. In this case we again want an as large as possible temperature difference over the GMR stack.

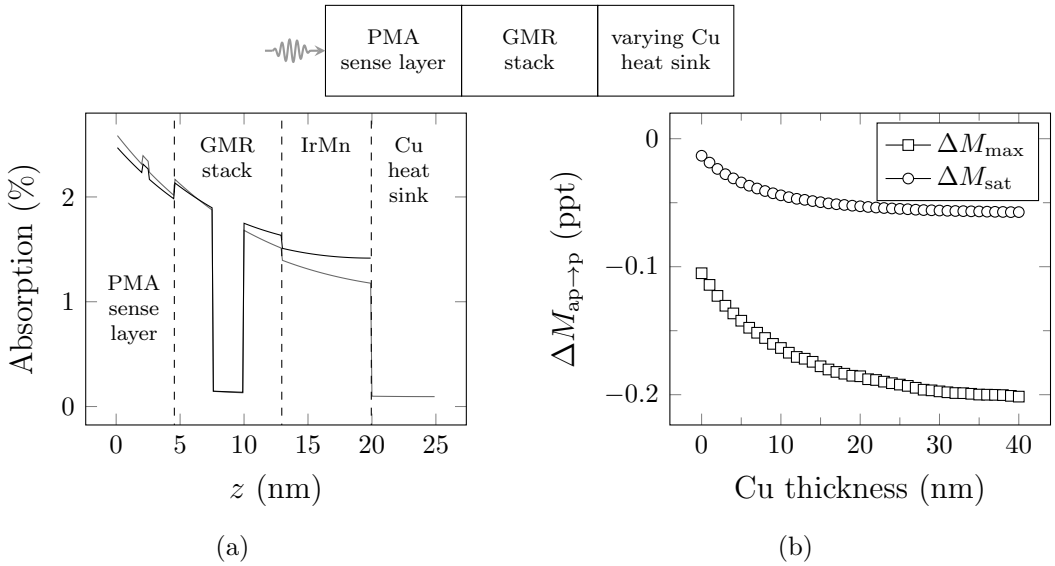

Figure 5.4: (a) Absorption per nm for the device with and without a Cu heat sink. (b) Difference in demagnetization in percentage points when the device is switched to the parallel configuration. Both the difference in the maximum and in the saturation value are shown.

Again, only the addition of a heat sink will have a beneficial effect on the size of the demagnetization. An example absorption profile is shown in Fig. 5.5 (a). The resulting changes in the demagnetization are shown in Fig. 5.5 (b), again in percentage points.

There is now a maximum in the change in demagnetization as a function of copper thickness. This is due to the fact that more copper again causes more heat to flow through the GMR stack, but since the copper layer is placed in between the GMR stack and the top layer it also absorbs part of the heat flowing through the GMR stack. Therefore there is an optimal copper thickness, in this case around 5 nm.

The curves shown in Fig. 5.3 are the demagnetization curves of a device with a heat sink of 40 nm for the frontpump and 5 nm for the backpump setup, and thus show the maximum difference achieved in these simulations. For the frontpump setup the total demagnetization for antiparallel alignment is 3.9 %, giving a relative change when switching to parallel alignment of −5.5 %. For the backpump setup the total demagnetization is 2.9 %, giving a relative difference of 5.6 %.

Finally, Fig. 5.6 shows the relative difference between parallel and antiparallel alignment for both the front- and backpump setup as a function of time for different copper thicknesses. In both setups transport behaves similar. The main contribution of the diffusive transport happens in the first 500 fs, which is com-

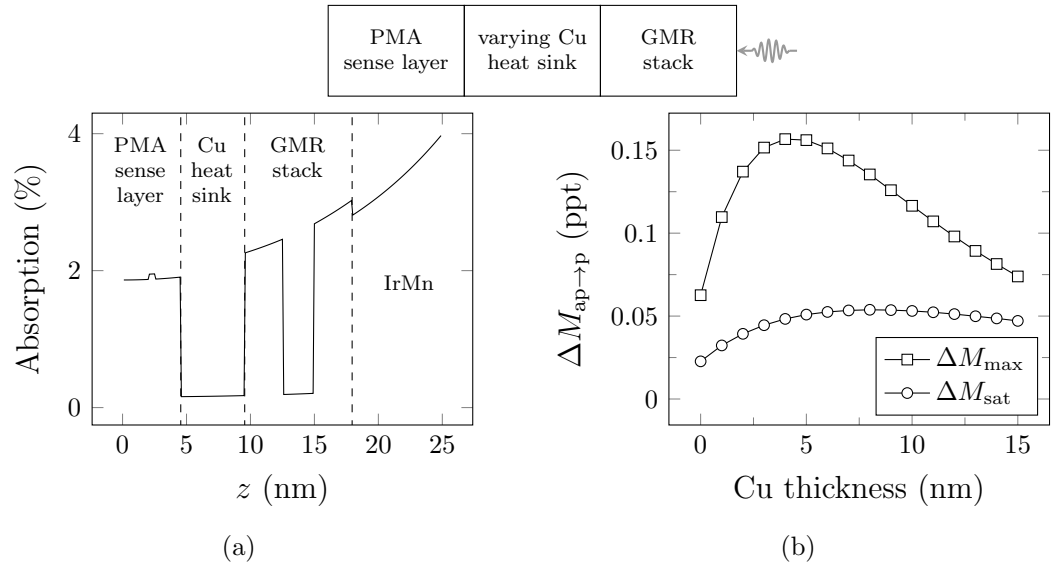

(a) (b)

Figure 5.5: (a) Absorption per nm for the device when heated from the back. (b) Both the difference in the maximum and in the saturation value of the demagnetization in percentage points when the device is switched to the parallel configuration.

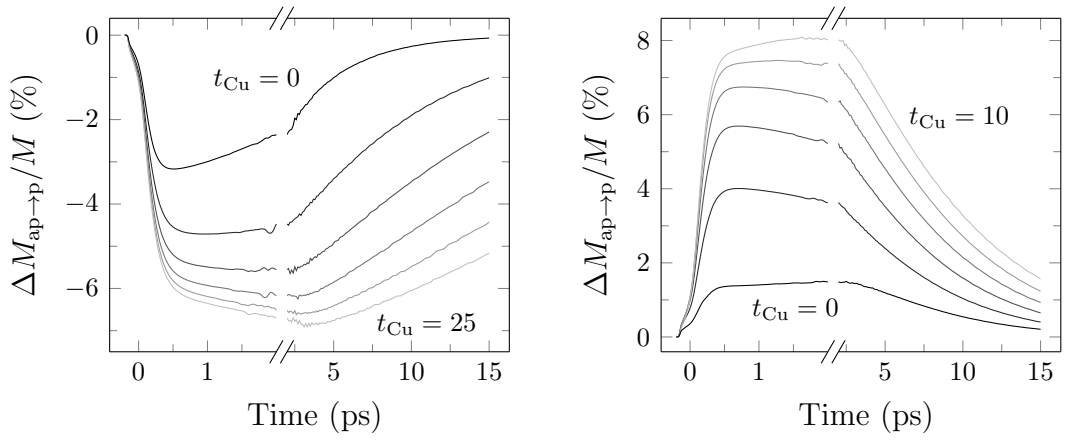

(a) (b)

Figure 5.6: Relative increase in demagnetization when switching to the parallel configuration as a function of time for (a) front- and (b) backpump setup, and for different Cu thicknesses.

parable to the demagnetization process. Therefore it is not expected that the GMTR will have a large effect on the timescales involved. The difference then slowly disappears again at larger timescales of several picoseconds.

5.3 Ballistic Transport

The next step is to investigate the effects of GMTR if ballistic transport would be dominant in these devices. In this case electrons that are excited by the laser will move through the device with the fermi velocity v_{F}, after which they deposit their excess energy through scattering. In Ref. 35 it has been shown that the resulting heat profile can be written as:

$$n_\delta(z,t) = \frac{N e^{-\frac{v_{\mathrm{F}} t}{\lambda} - \frac{t}{\tau}}}{2 v_{\mathrm{F}} t} \cdot \begin{cases} e^{\frac{z}{\lambda}} \left(e^{\frac{v_{\mathrm{F}} t - z}{\lambda}} - 1 \right) + e^{-\frac{z}{\lambda}} \left(e^{\frac{v_{\mathrm{F}} t + z}{\lambda}} - 1 \right) & z \leq v_{\mathrm{F}} t \\ e^{-\frac{z}{\lambda}} \left(e^{\frac{2 v_{\mathrm{F}} t}{\lambda}} - 1 \right) & z > v_{\mathrm{F}} t \end{cases} , \quad (5.3)$$

with N the total amount of excited electrons, λ the penetration depth of the laser, and τ the lifetime of the electrons. Ballistic transport can then be simulated by inserting this profile into the heating term of equation (5.1). However, this equation assumes a single material with a certain penetration depth. Therefore a Monte Carlo simulation was written to simulate the heat profiles resulting from the ballistic electrons in a more complex device.

In order to simulate these ballistic electrons, the following assumptions are made:

1. Electrons are excited proportional to the absorption profile, after which they start to move in a random direction with a speed $v_{\mathrm{F}} = 10^6\ \mathrm{m\,s^{-1}}$.
2. Ballistic electrons decay through scattering, after which they deposit all of their excess energy. Scattering occurs at a material-specific time scale τ, so that the chance P that an electron survives for a time t inside a material is given by $P = e^{-t/\tau}$.
3. Electrons reaching an interface between two materials before scattering have a chance to be reflected, inverting their direction. If they are transmitted, they will scatter according to the new material's scattering time.

Since simulations are done in one dimension, we are only interested in the z-components of the velocities. The first assumptions then gives a distribution which can be derived to be uniform:[35]

$$n_v(v) = \begin{cases} \frac{1}{2 v_{\mathrm{F}}} & |v| \leq v_{\mathrm{F}} \\ 0 & |v| > v_{\mathrm{F}} \end{cases} .$$

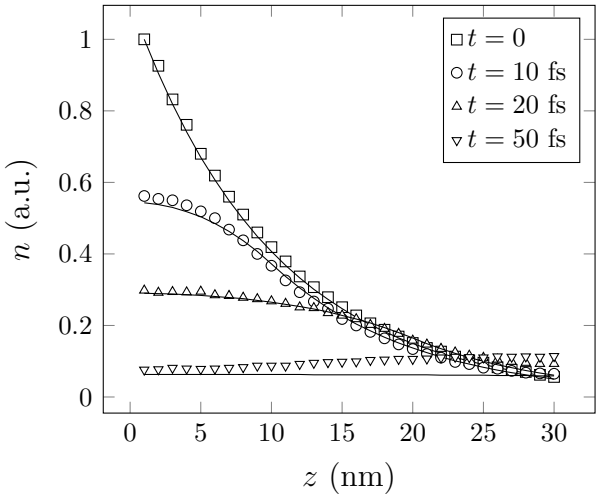

Figure 5.7: Ballistic electron density n inside a single material at four different times for $\tau = 40$ fs and $v_\mathrm{F} = 10^6\ \mathrm{m\,s^{-1}}$. The laser is assumed to decay exponentially inside the material with a penetration depth of $\lambda = 10$ nm. The symbols are results from the simulations, and the solid lines show the densities according to equation (5.3).

Electrons are therefore given a random uniformly distributed velocity, for which holds that $|v| < v_\mathrm{F}$. After creating these electrons, each one is given a random time-to-live before it decays. Following assumption 2 this time is given by

$$t = -\tau \cdot \ln P\,,$$

where P is now taken to be a random number between zero and one. If the combination of the time-to-live and velocity of the electron brings it beyond an interface, the electron is instead moved up to the interface. It is then tested if the electron is transmitted or reflected using a reflection coefficient depending on the materials at the interface, and the electron is given a new time-to-live for the rest of its path. At the edges of the device the electrons are always reflected.

Electrons then deposit all of their energy at the end of their path, resulting in a time and position dependent energy profile which can be inserted into the M3TM simulations. To speed up the simulations a maximum time-to-live is used so that approximately 1 % of electrons has their lifetime cut off, but since these electrons have already traversed the device several times, they are assumed to have no significant influence.

In order to validate the correctness of the simulations, the results for a single material with an exponential decaying absorption profile are compared to the values expected from equation (5.3). Figure 5.7 shows the resulting heat profiles at four

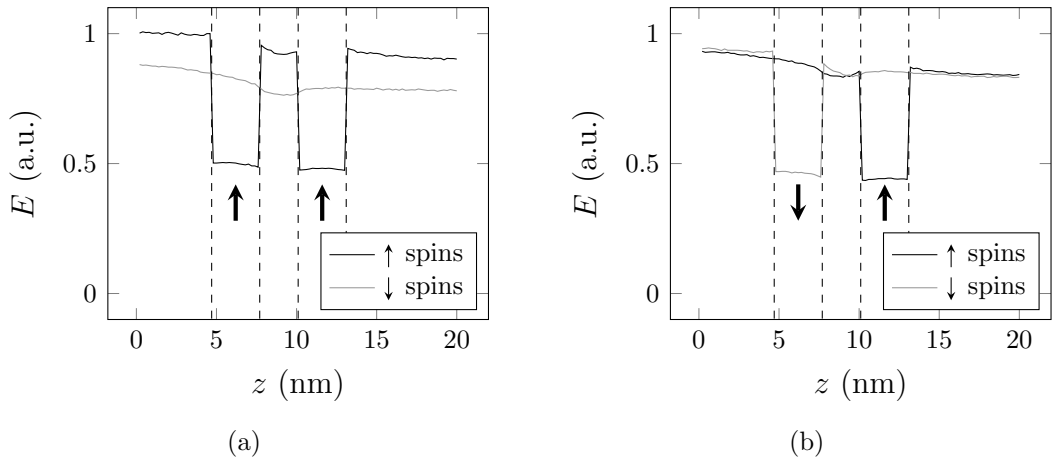

Figure 5.8: Energy deposited by ballistic electrons for both spin channels for (a) parallel alignment and (b) antiparallel alignment. Arrows indicate magnetization directions.

different times. Symbols represent the results from the simulations, solid lines the analytical solution. As can be seen, the simulations are in good agreement with the theory. The results start to deviate at the end of the sample after 20 fs, but this is expected since in the simulations electrons are reflected from the back of the sample while they are assumed to move through the substrate for the derivation of equation (5.3).

The next step is then to find a suitable way to describe the GMTR in these devices. For this, two different methods are investigated — either giving majority and minority carriers different lifetimes, or adding spin-dependent interface scattering. The results for these two methods will be discussed in the next two sections.

5.3.1 GMTR Through Different Lifetimes

First, the addition of spin-dependent lifetimes is investigated. Figure 5.8 shows the total energy deposited by the ballistic electrons as a function of position for both a parallel and an antiparallel configuration of the GMR stack. Black lines represent the up–electrons, gray lines the down–electrons. For these profiles the minority carriers have a lifetime of 40 fs, while the lifetime of majority carriers is increased to 80 fs. All electrons have a lifetime of 40 fs inside nonmagnetic layers. Note that this is the average time before complete thermalization, which is much higher than the time between two collisions mentioned in section 2.4.

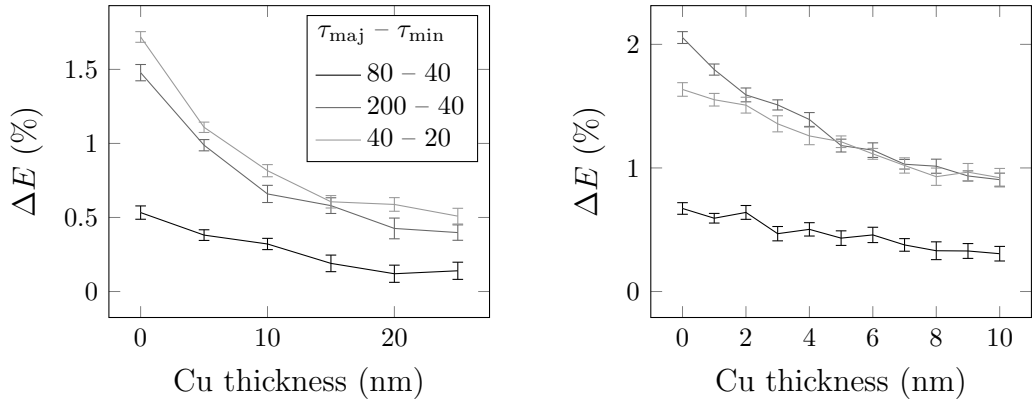

Figure 5.9: Difference in energy deposited in the top layer by ballistic electrons between antiparallel and parallel alignment for both the (a) frontpump and (b) backpump setup.

As can be seen from the profiles, majority carriers indeed deposit less energy inside the magnetic layers due to their decreased chance of scattering. As a result, more energy is deposited at other locations, due to the amount of deposited energy remaining the same. This will therefore result in different temperatures inside the top layer between parallel and antiparallel alignment.

The difference in deposited energy between antiparallel and parallel alignment is shown in Fig. 5.9 (a) for a few different lifetimes and for different thicknesses of the copper heat sink. The lifetime inside nonmagnetic materials remains 40 fs in all simulations. A strikingly different behavior can now be observed as compared to previous simulations: as the device switches to a parallel alignment, the temperature in the top layer increases. This is due to the fact that it now becomes more likely for electrons to traverse the entire device. This allows more electrons to flow into the top layer in the case of parallel alignment. However, since there is no confinement of ballistic electrons, the amount of electrons flowing out of the top layer remains the same, resulting in a higher temperature. Adding copper to the device reduces the amount of electrons reaching the top layer, therefore decreasing this effect.

However, the problem with the picture sketched above is that the difference in temperatures arises due to electrons flowing from the cold to the hot side. This is because the average distance an electron moves within 40 fs is 20 nm, which is the same as the size of the device, allowing the electrons to easily deposit all their energy at large distances. This is assumed to be unrealistic, since electrons have

Table 5.1: Transmission probabilities for both majority and minority carriers when moving from Cu to Co and from Co to Cu.

from / to	maj.	min.
Cu / Co	0.73	0.54
Co / Cu	0.94	0.33

much smaller mean-free-paths, so that they slowly deposit their energy along the way. Furthermore, electrons at the hot side are expected to be confined due to the scattering, which is again not the case in the simulations.

These problems could be solved by decreasing the scattering time to prevent electrons from traversing the device easily, but in this case a difference is no longer expected when switching the GMR stack. We therefore conclude that the assumption that electrons only deposit their energy once after a certain average thermalization time provides unrealistic results when combined with a GMTR effect through spin-dependent lifetimes.

Figure 5.9 (b) shows the difference in energy deposited in case of the backpump setup. These results are in better agreement with the other models, since now an increase in temperature is expected when switching to parallel alignment. However, the effects mentioned before are still present, making the results questionable.

5.3.2 GMTR by Interface Scattering

The second method of adding a GMTR effect to the ballistic electrons is to add spin-dependent interface scattering. In this case, electrons no longer travel in one direction, so that the approximation that electrons deposit their energy once after an average thermalization time is no longer expected to give unrealistic results. Table 5.1 shows the transmission probabilities found from literature for Co / Cu interfaces.[37] The same values were also taken for interfaces of other materials with cobalt since the spin-dependency is mostly caused by the cobalt.

Resulting energy deposition profiles are shown in Fig. 5.10. Again, both parallel and antiparallel alignment are shown, with black curves corresponding to up–electrons and gray to down–electrons. As can be seen from these graphs minority carriers deposit more energy inside the magnetic layers, while majority carriers deposit less energy. Since lifetimes are kept constant throughout the device — again chosen to be 40 fs — the deposited energy corresponds to the ballistic electron density. The main effect of the interface scattering is thus to confine minority electrons inside the magnetic layers, while majority electrons move through these layers more easily, as expected from the values of Table 5.1.

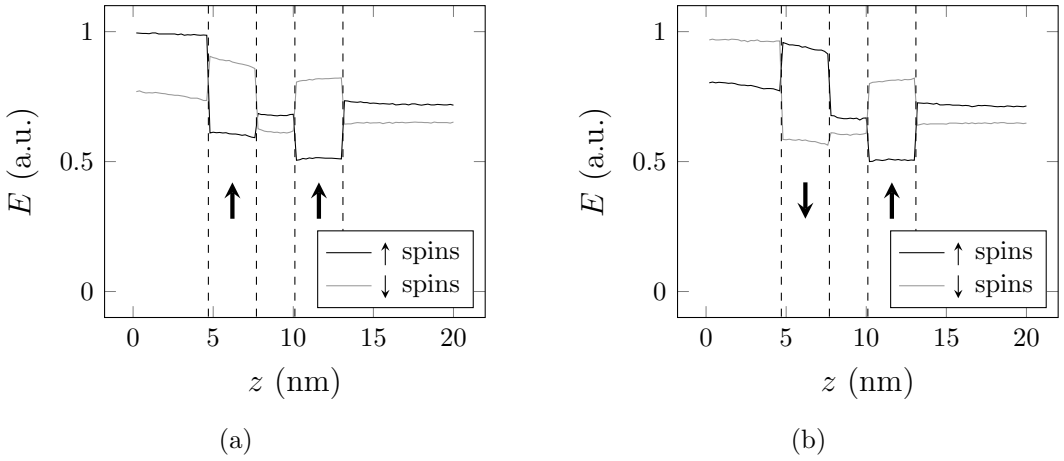

Figure 5.10: Energy deposited by ballistic electrons for both spin channels for (a) parallel alignment and (b) antiparallel alignment. Arrows indicate magnetization directions.

Figure 5.11 shows the difference in energy deposited in the top layer between parallel and antiparallel alignment for both the frontpump and the backpump setup. As expected, we now find a decrease for the frontpump, and an increase for the backpump setup. Both the effects increase when more copper is added. The increase when copper is added in the backpump setup is not straightforward, since heat transport no longer depends on a temperature difference. Closer inspection of the energy profiles shows that the main contribution from the copper is to decrease the amount of electrons being excited in the top layer. Since these travel away more easily in the parallel alignment, they counteract the effect. Therefore the addition of the copper will give a larger increase in temperature.

Using these temperature profiles, the demagnetization can now be simulated. However, since all of the ballistic electrons will have been removed after several picoseconds, this will give unrealistic temperature profiles at large timescales. Therefore, diffusion is still included after the ballistic electrons have deposited their energy. Total transport of heat is thus the sum of excited electrons moving ballistically through the sample, and diffusion of the heat deposited by these electrons. Diffusion is now taken to be independent of magnetic layer alignment.

Figure 5.12 shows the difference in demagnetization as a function of time for varying copper thicknesses for both the frontpump and the backpump setup. The dashed line shows the difference when diffusion is neglected. In this case, we find a slightly larger maximum, but also a difference that remains constant over long timescales. Compared to Fig. 5.6, ballistic transport will cause a faster increase in

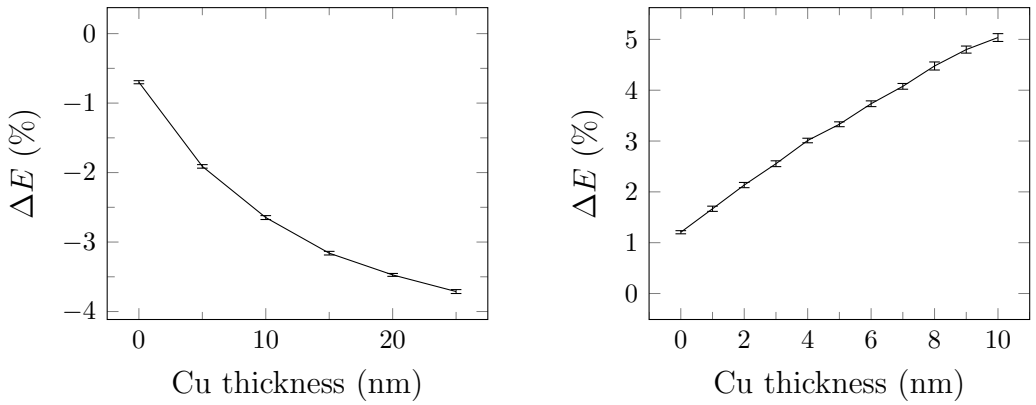

(a) (b)

Figure 5.11: Difference in energy deposited in the top layer by ballistic electrons between antiparallel and parallel alignment for both the (a) frontpump and (b) backpump setup.

demagnetization, but the effect will also cease earlier, so that diffusion will cause the effect to diminish faster.

The maximum difference in the total demagnetization is shown in Fig. 5.13, again in percentage points. Just as with diffusive transport, the addition of a copper heat sink increases the effect for the frontpump setup, and for the backpump setup both increases the relative temperature difference, but also hinders transport, resulting in an optimal thickness around 6 nm. The difference is approximately the same as with diffusive transport if a change in heat conduction of 50 % would have been chosen.

To conclude, the influence of the GMTR effect on ballistic electrons has been investigated. The GMTR has been simulated in two different ways, namely through spin dependent lifetimes and spin dependent interface scattering. Due to the way ballistic electrons are treated in the simulations, the results of spin dependent lifetimes are assumed to be unrealistic. The addition of interface scattering does give realistic results, where a comparable effect on the demagnetization has been found as with the simulations on diffusive transport, but on slightly faster timescales.

5.4 Superdiffusive Transport

Finally, transport in the superdiffusive regime is investigated, where ballistic electrons can transfer their energy to other electrons, exciting them above the Fermi

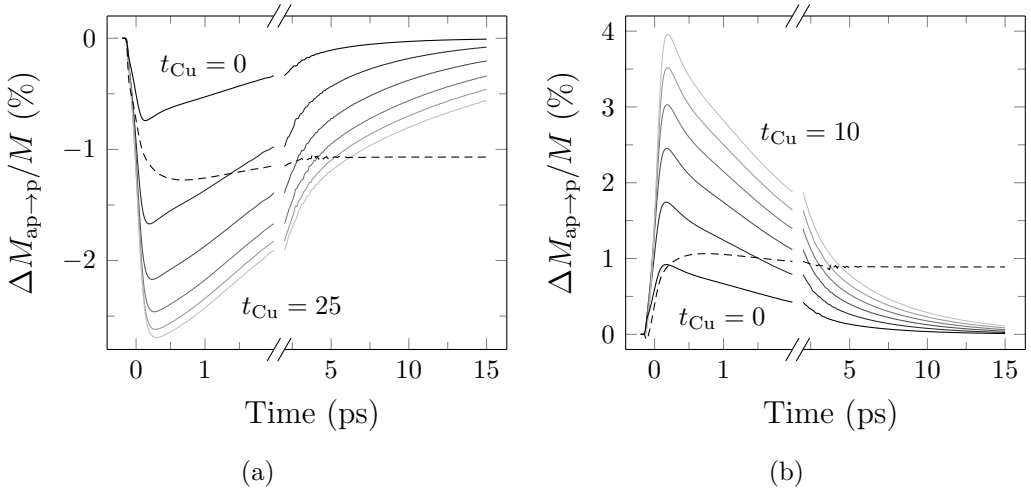

(a) (b)

Figure 5.12: Relative increase in demagnetization when switching to the parallel configuration as a function of time for different Cu thicknesses for (a) the frontpump and (b) the backpump setup. The dashed line shows the case without diffusion of the deposited heat in the case of $t_{\mathrm{Cu}} = 0$.

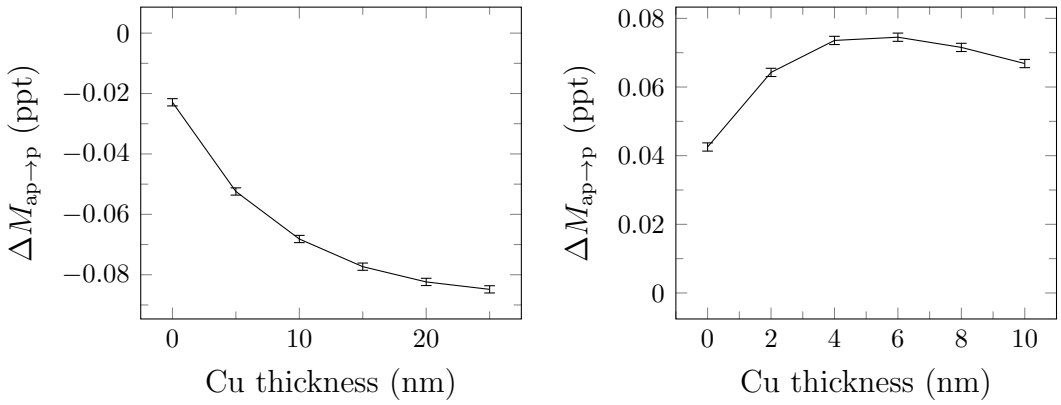

(a) (b)

Figure 5.13: Difference in the maximum demagnetization between parallel and antiparallel alignment in (a) front- and (b) backpump setup for both ballistic and diffusive transport.

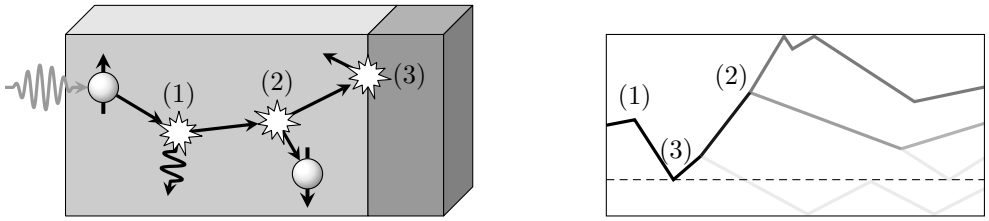

(a) (b)

Figure 5.14: (a) After excitation by the laser, electrons start to move through the device. They then either scatter (1) elastically with the lattice, or (2) inelastically with electrons below the Fermi level, exciting them. When reaching an interface, electrons have a chance to be reflected. (b) Example of the simulated trajectories with one excited electron, showing the three types of scattering. The dashed line denotes an interface with a transmission probability of 50 %. Darker lines represent electrons with higher energy.

energy. In this way, shortly after laser excitation transport is governed by cascades of electrons.

Energy profiles are again calculated using Monte Carlo simulations. All assumptions about non-equilibrium electrons are similar to those made by Battiato *et al.*[11] However, contrary to Ref. 11, demagnetization is assumed to be due to heating instead of spin-polarized electron transport.

Figure 5.14 (a) illustrates how electrons move through the device. Electrons are first excited by the laser pulse, giving them a random energy between 0 and 1.6 eV above the Fermi energy. They then move through the device in a random direction, until they either (1) scatter with phonons or impurities, or (2) with other electrons around the Fermi level. Scattering with the lattice is approximated as elastic scattering, and independent of the incoming direction. Scattering with other electrons is inelastic, exciting the second electron. The new trajectories are then calculated using conservation of energy and momentum. When hot electrons reach the interface, there is a chance to be reflected as in (3). In Fig. 5.14 (b) an example of a simulated trajectory is shown for a device with one interface, showing all three types of scattering.

Electron lifetimes and velocities are assumed to be energy dependent. As explained in section 2.4, the characteristic electron–electron scattering time is given by

$$\tau_{ee} = \frac{1}{K_{ee}(E - E_{\mathrm{F}})^2} ,$$

with $1/K_{ee}$ typically having a value of several $\mathrm{fs\,eV^2}$.

Electron–phonon scattering is assumed to follow a similar behavior, and its scattering constant is taken to be the same as for e–e scattering for simplicity. Effectively, this yields a twice as small characteristic time until *any* scattering event, which is then randomly assigned to be either an e–e or an e–p scattering event, both having an equal probability.

In Ref. 11 electrons are assumed to have zero velocity slightly above the Fermi energy due to holes counteracting any transport effects. The velocity is approximated as

$$v = v_0 \sqrt{(E - E_\mathrm{F})}\,,$$

with $v_0 = 10^6\ \mathrm{m\,s^{-1}}$. These two equations are reasonable approximations of the lifetimes and velocities used in Ref. 11. Note that the square root behavior of the velocity has no physical meaning, but is purely used as a simple fit to the actual values.

All types of transport discussed here can be characterized by the variance σ of the displacement, which is defined along the z-axis as

$$\sigma^2 = \int n(t,z)(z - z_0)^2\,\mathrm{d}z\,.$$

The variance can also be written in terms of the anomalous diffusion exponent γ as

$$\sigma^2 \propto t^{2/\gamma}\,.$$

Diffusive transport can be described with $\gamma = 2$, ballistic transport with $\gamma = 1$.

Figure 5.15 (a) shows the variance as a function of time for a delta peak initial distribution for several lifetimes. With almost no scattering, the electrons move ballistically through the sample. By decreasing their mean-free-path, the transport will slowly shift from the ballistic regime to the diffusive regime at longer timescales. This can be seen from Fig. 5.15 (b), where the second derivative is plotted. With no scattering it stays constant, corresponding to $\gamma = 1$. With scattering it slowly decreases, reaching zero for $t \gg \tau$ which corresponds to $\gamma = 2$. The simulations thus work as expected.

From these simulations we can again extract an energy profile, which can be inserted into the heating term of equation (5.1). For this energy profile, the total amount of energy stored in the excited electrons is used. Figure 5.16 shows the energy profile inside the device during the first 200 fs in the case of $\tau = 10$ fs when heated from the back. As can be seen, the initial absorption profile will rapidly disappear through the ballistic transport of the highly energetic electrons.

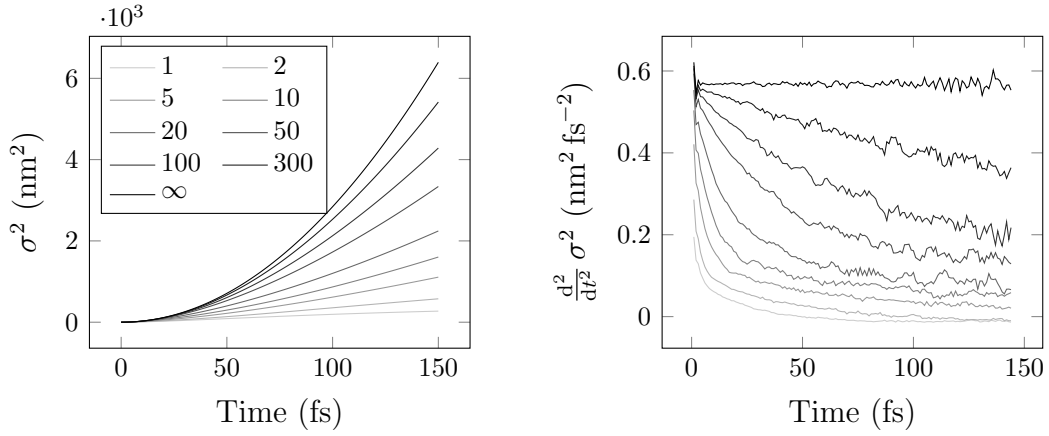

(a) (b)

Figure 5.15: (a) Variance of the position for a single particle distribution versus time for different scattering times. (b) Second derivative, showing that transport indeed changes from $d_w = 1$ to $d_w = 2$.

However, after 200 fs one side of the device will remain hotter than the other, and this will equilibrate on much slower timescales, due to the electrons slowing down. Furthermore, the amount of electrons inside the GMR stack remains larger, since minority electrons will be trapped here due to interface scattering.

Figure 5.17 again shows the difference in energy deposited in the top layer between a parallel and antiparallel alignment, shown as a function of time for a few different copper thicknesses. For simplicity, lifetimes are assumed to be spin-independent, and the GMTR effect is taken into account through interface scattering. For the frontpump setup an increase in temperature is seen on short timescales due to ballistic electrons. However, the diffusive character quickly takes over, leading to a decrease at longer timescales when a copper heat sink is added. For the backpump setup, we only see an increase, mainly on short timescales. Adding more copper increases the effect, and slightly delays the increase in heat, as can be expected.

For both the frontpump and backpump the difference slowly disappears again after several hundreds of femtoseconds. A demagnetization is still expected to be visible, since this difference is further smeared out over 70 fs due to the finite pump pulse, making the difference exist well beyond the start of the demagnetization process. However, this has not been verified with the simulations, since the resulting temperature profiles have too much noise to use to accurately simulate the demagnetization.

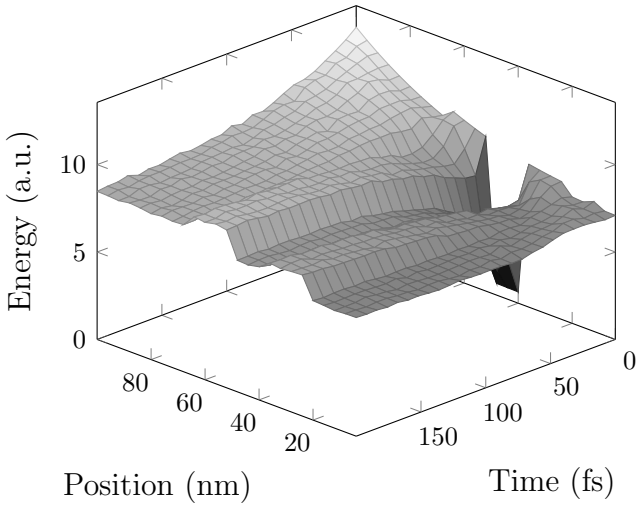

Figure 5.16: Energy profile in the device during the first 200 fs after laser excitation for $\tau = 10$ fs.

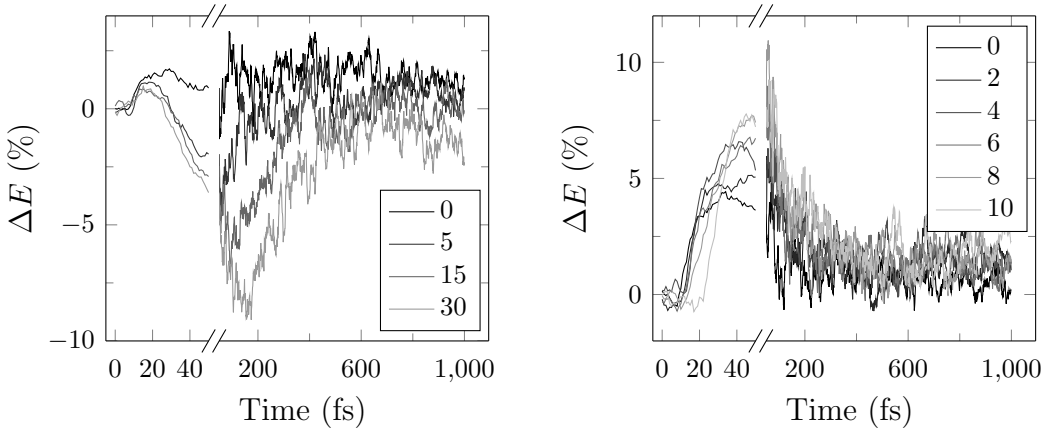

Figure 5.17: Difference in energy deposited by superdiffusive electrons as a function of time for various Cu heat sink thicknesses for (a) frontpump and (b) backpump setup.

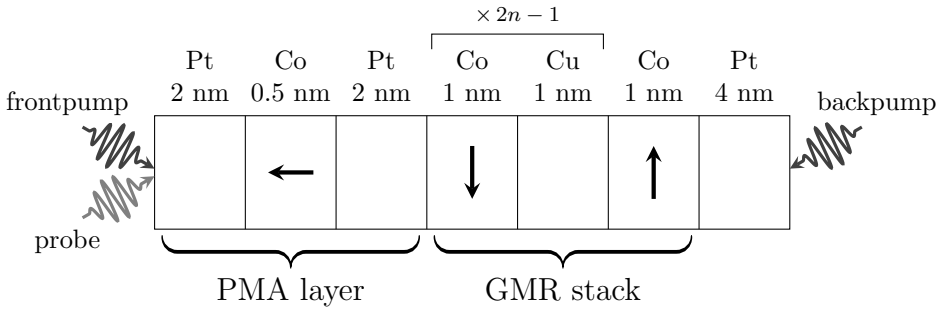

Figure 5.18: Device layout of the multilayer stack. The amount of repetitions of the two Co layers is denoted by n.

Compared to diffusive and ballistic transport, superdiffusive transport will cause the effect to disappear much faster. Adding spin-dependent lifetimes might solve this problem by making the diffusive behavior dependent on the configuration — in Ref. 11 this causes differences in spin up and down electrons for much longer timescales — but this has not been done due to the complexity of the simulations.

To conclude, a measurable effect is expected for all types of transport. Adding a copper heat sink will increase this effect. Both ballistic and diffusive transport give comparable results, but on slightly different timescales. For superdiffusive transport we also expect an effect, but due to the complexity of the simulations not much can be said about how this compares to the other types of transport.

5.5 Multilayer GMR Stacks

A different way of creating GMR stacks is through the RKKY interaction. In these stacks the cobalt layers are separated by a thin spacer layer of a certain thickness. At a certain spacer thickness the cobalt layers will prefer an antiparallel alignment due to this RKKY interaction. The alignment can then be altered using an external magnetic field. The main advantages of such a device are that the relatively thick iridium manganese layer is no longer needed, and that the stack can easily consist of more than two cobalt layers, therefore providing an extra degree of optimization. However, due to difficulties in fabricating these devices they were not used for the experiments.

Again, the device consists of a perpendicularly magnetized top layer consisting of Pt (2 nm) / Co (0.5 nm) / Pt (2 nm), placed on top of a multilayer GMR stack which consists of [Co (1 nm) / Cu (1 nm)]$_{2n-1}$ / Co (1 nm), with n the amount of

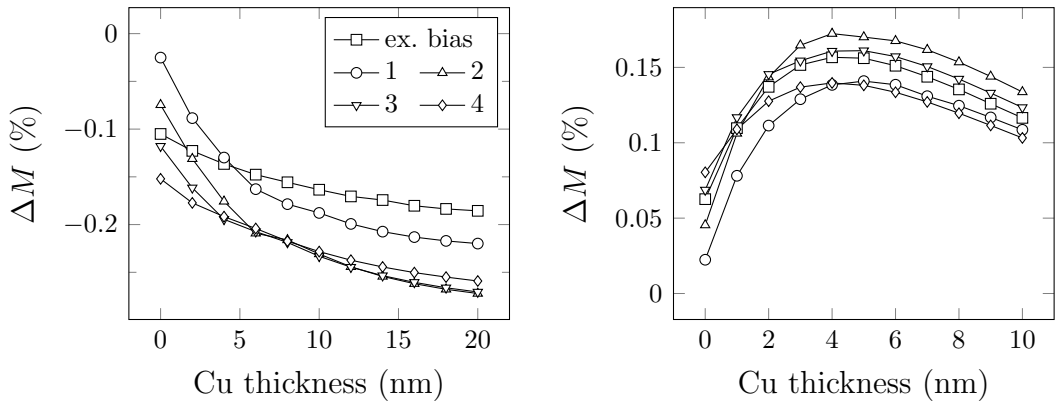

Figure 5.19: Difference in maximum demagnetization for the exchange biased stack, and for multilayered devices consisting of 1 to 4 repetitions for (a) frontpump and (b) backpump setup for diffusive transport.

repetitions. The entire device is then placed on a platinum buffer layer. Figure 5.18 shows the layout of the device.

In the next part, these devices will be compared to the exchange biased device. Due to the complexity in the superdiffusive simulations, only diffusive and ballistic transport will be considered.

5.5.1 Diffusive Transport

First, diffusive transport is investigated. The results for both the frontpump and the backpump setup are shown in Fig. 5.19 for different amount of singe GMR stacks, and for different copper heat sink thicknesses. Previous results for the exchange biased stack are also shown.

As can be seen from the frontpump simulations, without a heat sink the effect is larger with more GMR stacks. However, the effect of the copper is larger with less repetitions, therefore resulting in an optimum at two or three repetitions. The exchange biased stack shows a smaller effect, due to the thick iridium manganese layer in between the cobalt layers and the heat sink.

For the backpump setup we again see a larger effect in the multilayered stack, although the difference is now smaller, and an optimum is again found, this time for two repetitions. These results are for a platinum buffer layer of 4 nm. However, these values change for different buffer layer thicknesses. Table 5.2 shows

Table 5.2: Optimal Cu and Pt thicknesses for devices consisting of 1 to 4 repetitions, together with the maximum difference in demagnetization.

n	Cu (nm)	Pt (nm)	ΔM (%)
1	5	4	0.140
2	5	3	0.178
3	5	2	0.172
4	4	2	0.153

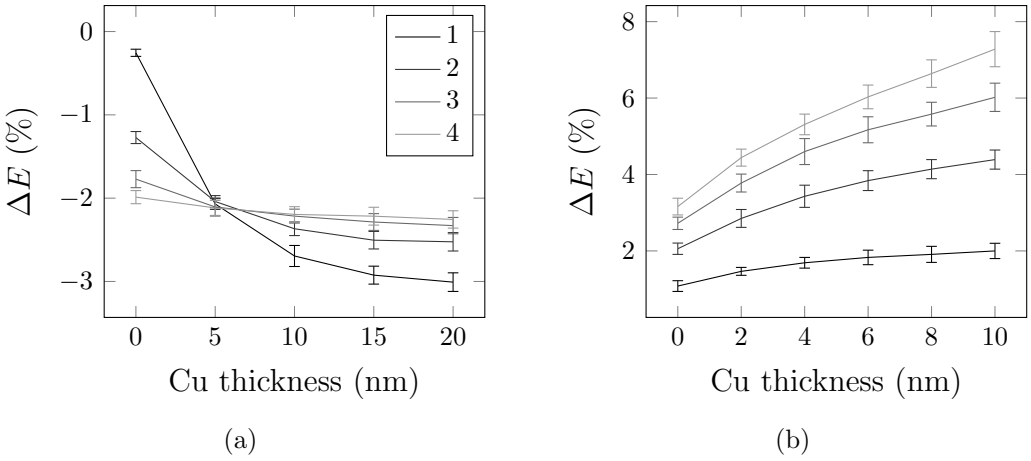

Figure 5.20: Difference in energy deposited in the top layer for (a) frontpump and (b) backup setup for devices with 1 to 4 repetitions for ballistic transport.

the optimum values of both the platinum and copper thickness for all 4 devices, together with the maximum difference.

These results show that for diffusive transport, multilayered stacks are indeed a better candidate to measure the effect, due to the absence of the iridium manganese, and the ability to tune the thickness of the GMR stack, as expected.

5.5.2 Ballistic Transport

Finally, the difference between all devices in the case of ballistic transport is examined. Only spin-dependent interface scattering is taken into account. Furthermore, for simplicity the buffer layer is now kept at 4 nm. Figure 5.20 shows the resulting differences in deposited energy in the top layer for both the frontpump and backpump setup. Both behave comparable to the exchange biased stack.

For the frontpump setup, the addition of more repetitions will increase the effect without a heat sink, but decrease the maximum effect, since the larger GMR stack now prevents the electrons from reaching the copper. For the frontpump measurements the use of a multilayered stack is therefore not expected to improve the effect in case of ballistic transport.

This is not the case for the backpump setup, where adding more repetitions results in a larger effect. The addition of more repetitions does decrease the demagnetization in this case, so that an optimum is again expected.

To conclude, for multilayered GMR devices the effects are expected to behave similar, but due to the possibility of tuning the amount of repetitions, a better optimization is possible. However, due to the difficulty in fabricating these devices, all measurements shown in the next chapter were done on exchange biased devices.

Chapter 6

Controlling Heat Transport

In this chapter measurements on the GMTR effect are presented. First, the fabrication steps for creating a working device are presented. The device consists of a perpendicularly magnetized layer placed on top of a GMR stack. The optimum growth parameters for the GMR stack are investigated first, after which the magnetic properties of the the out-of-plane layer are tailored. Next, pump–probe measurements are presented using two different configurations of the TR-MOKE setup. It is unambiguously shown that it is indeed possible to control heat transport on ultrashort timescales using a spin-valve. Furthermore, it is shown that only one of the two measuring methods used is suitable to separate the effect from other measurement artifacts.

6.1 Sample Fabrication

6.1.1 GMR stack

The first step of fabricating a working device is growing a GMR stack with an as large as possible MR ratio in order to maximize the GMTR effect. The device layout for the GMR stack was chosen to be IrMn / Co / Cu / Co (listed from top to bottom), where the top cobalt layer is pinned by an exchange bias with the iridium manganese. This layout was chosen due to its ease of processing, as compared to multilayers coupled through the RKKY effect. Furthermore, a buffer and a capping layer of 2 nm of platinum were used. Substrates were chemically cleaned using an ultrasonic bath for 10 minutes with ammonia, acetone and isopropanol. Substrates were then exposed to a 15 W oxygen plasma for 5 minutes.

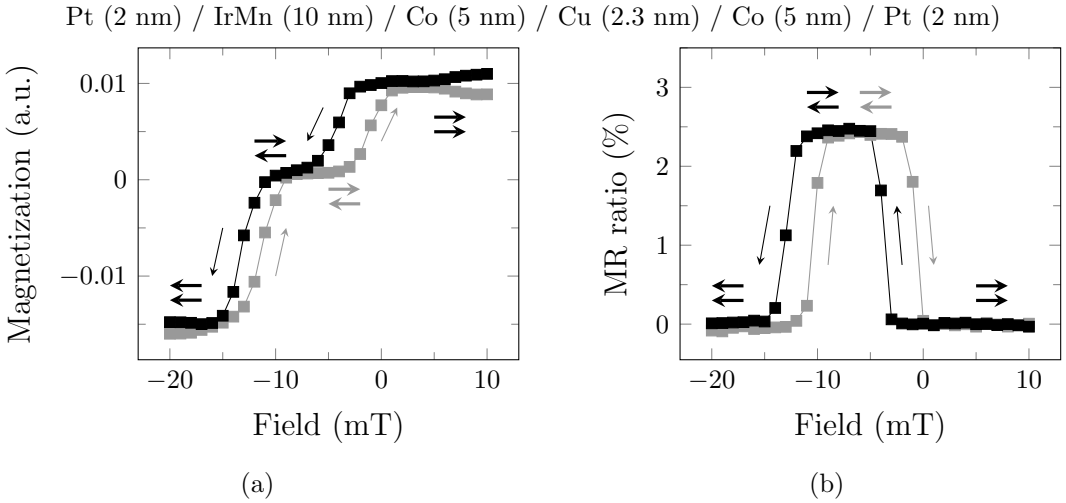

Figure 6.1: (a) Magnetization and (b) MR ratio of a GMR stack as a function of magnetic field. Thin arrows denote field sweep direction, while thick arrows show the orientation of the two magnetic layers.

For a more detailed study of the optimum cleaning steps and buffer and capping layers the reader is referred to the master thesis by P. Janssen.[38] Note that the vacuum annealing step was skipped, since this had no noticeable effect on the MR ratio for our samples.

Figure 6.1 (a) shows a typical hysteresis loop measured using a MOKE setup. The large step corresponds to the switching of the top exchange biased layer. The switching field of this pinned layer has shifted by 15 mT, making it possible to achieve both the parallel and the antiparallel configuration.

Figure 6.1 (b) shows the MR ratio when sweeping the magnetic field back and forth. The resistance is measured in the current in plane configuration, using a four point probe setup. The resistance is indeed large in the antiparallel configuration, and lowered in the parallel configuration. The MR ratio is only approximately 2.5 %, while in Ref. 38 an MR ratio of more than 7 % was achieved with a comparable device layout. Unfortunately we were unable to reach the same MR ratio despite using the same sputter deposition system under the same conditions as in Ref. 38, but the exact reason for this is unknown. However, since the device will be used in the current perpendicular to the plane configuration, which yields a higher ratio, and since the GMTR ratio is also expected to be higher, the MR ratio in our devices will turn out to be large enough to measure the desired effect.

Theoretically, for small copper thicknesses (usually smaller than 2 nm) the two cobalt layers are no longer decoupled, and little to no MR ratio is expected.

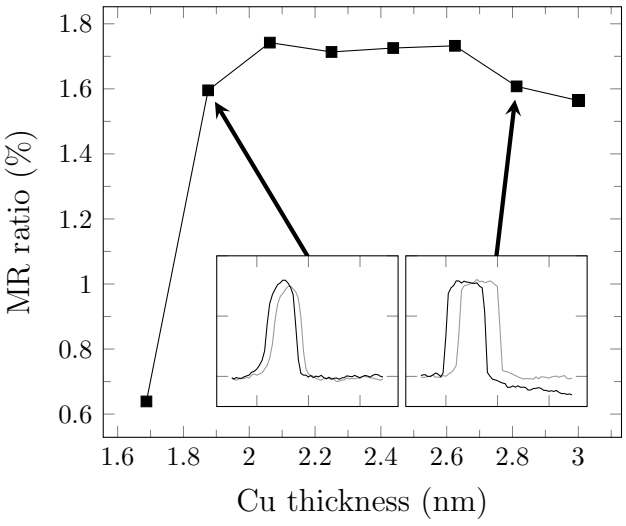

Figure 6.2: MR ratio for devices with different copper spacer layer thicknesses. The insets show the MR as a function of magnetic field, showing that below the maximum the two Co layers are coupled, and decouple above this value, as expected.

For large thicknesses, increasing the amount of copper will increase the chance of spin flip scattering, again decreasing the MR ratio. Therefore a maximum is expected.[39,40] Figure 6.2 shows the MR ratio for varying copper spacer layer thicknesses. We indeed find a maximum at a certain copper thickness. Furthermore, as the inset shows, the cobalt layers become coupled below this thickness, so that there is no longer a sharp transition to the antiparallel configuration. The optimum thickness is located between 2.1 and 2.6 nm, but is hard to determine accurately due to the large deviations between subsequent measurements. Therefore the optimum thickness is assumed to be 2.3 nm, just as in Ref. 38.

Figure 6.3 shows the MR for 4 devices with varying cobalt layer thicknesses. Decreasing the thickness causes the exchange field to increase. This is expected, since the exchange bias is an interface effect and is independent of the thickness, while the Zeeman contribution is proportional to the thickness.

The MR ratio remains approximately constant. The small differences in MR ratio are not attributed to a stronger GMR effect, but to other effects, such as different sample size and measuring conditions, which change the amount of current shunting. It is also not expected that the MR ratio changes significantly at these thicknesses.[39] Since the goal is to measure heat transport through the device, a thinner GMR stack is then desirable. However, easy switching of the magnetic lay-

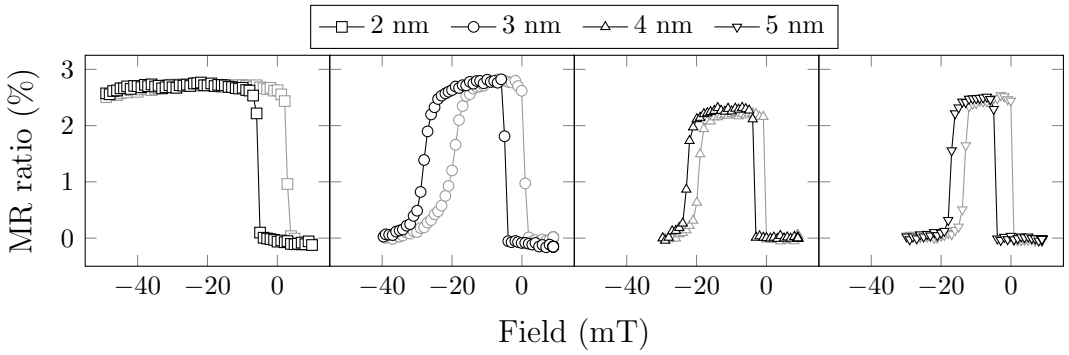

Figure 6.3: MR curves for different cobalt thicknesses.

ers is also desired, which is not the case for the 2 nm pinned cobalt layer, making a cobalt thickness of 3 nm preferable.

6.1.2 GMTR Device

Now that the optimum thickness for each layer of the GMR stack has been found, the complete device can be fabricated. This device consists of a magnetic sense layer placed on top of the GMR stack, and a copper heat sink placed either on the bottom for measurements where the sample is heated from the front, and in between when heating from the back, similar to sections 5.2–5.4. For the sense layer Pt / Co / Pt was used, which has a perpendicular magnetic anisotropy (PMA), and shows a relatively large magneto-optical contrast.

The minimal iridium manganese thickness for a working exchange bias at room temperature is approximately 4 nm,[41] but since the sample will be heated by a pump pulse, a thickness of 7 nm was chosen. To improve heat transport through the GMR stack, the iridium manganese is also placed at the bottom. The exchange bias is now accomplished by heating to a temperature above the blocking temperature, and cooling down inside an external magnetic field. Blocking temperatures for these thicknesses are around 200–250 °C.[42–45] However, annealing close to the blocking temperature is typically done for several hours. Since annealing to higher temperatures doesn't influence the MR ratio,[46] samples were annealed to 300 °C for 5 minutes, with a ramp time of 30 minutes, after which they were cooled inside a magnetic field. Since perpendicular magnetization disappears at high temperatures due to interdiffusion of the layers,[47] annealing was done in situ before depositing the PMA layer. To prevent the top cobalt layer from oxidizing during this annealing, an additional platinum capping layer of 1 nm was placed in between the GMR stack and the PMA layer.

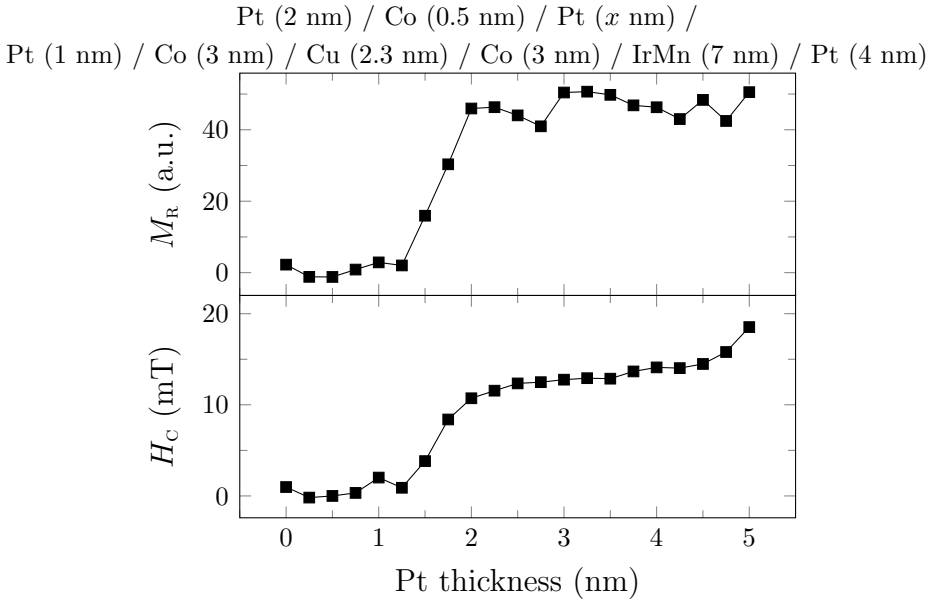

Figure 6.4: Out-of-plane remanence and coercivity of the device with varying Pt buffer layer thickness for the PMA top layers.

For the PMA layer a cobalt layer with a thickness of 0.5 nm sandwiched between two platinum layers was used. Figure 6.4 shows both the remanence and coercivity of the out-of-plane layer as a function of platinum buffer layer thickness when grown on top of a GMR stack. Starting at a thickness of approximately 2–2.5 nm the cobalt will become perpendicularly magnetized. Note that this is on top of the 1 nm platinum capping layer, which has presumably diffused into the cobalt layer during the annealing.

A copper heat sink with a varying thickness was also added to the device. However, this heat sink will not be used in the measurements shown in section 6.2.1. The reason for this is that when the copper is placed on the bottom of the device, it hinders the growth of the GMR stack. This is shown in Fig. 6.5 (a), where the longitudinal MOKE signal is shown at a few different copper thicknesses. As can be seen, the hysteresis loops of both cobalt layers slowly shift towards each other until they become fully coupled at large copper thicknesses. Figure 6.5 (b) shows the magnetic field range where the forward and backward sweep have the same value, which serves as a measure of how well-defined the antiferromagnetic state is. This width immediately decreases even when a little copper is added, until it completely vanishes after 30 nm. Therefore all measurements where the sample is heated from the front were only done on the region with no copper on the bottom.

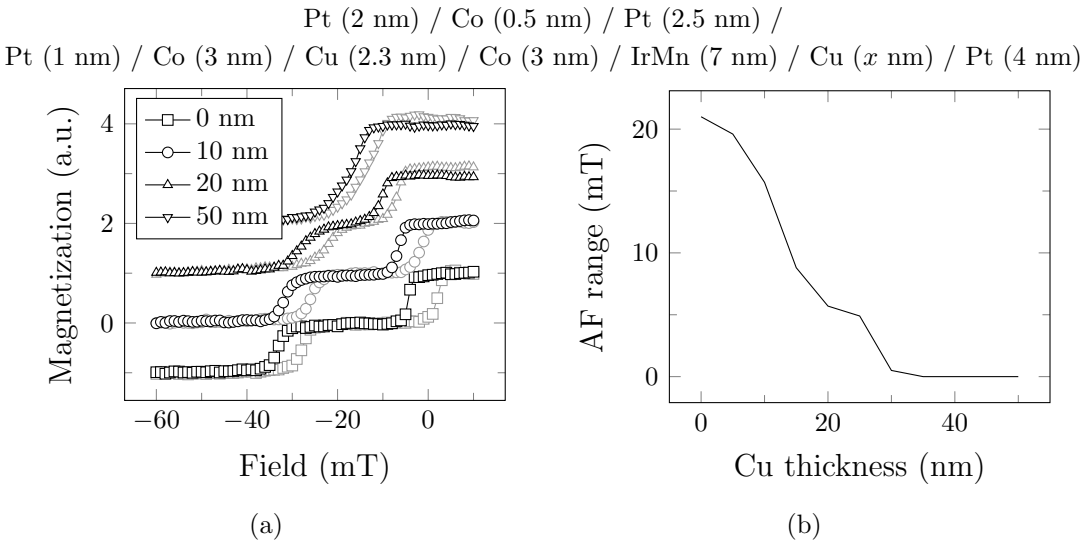

Figure 6.5: (a) In-plane magnetization for several Cu thicknesses, shifted for better visibility. (b) Magnetic field range where the two in-plane Co layers are in the AF configuration in both the forward and backward sweep, showing that the two layers start to couple at larger Cu thicknesses.

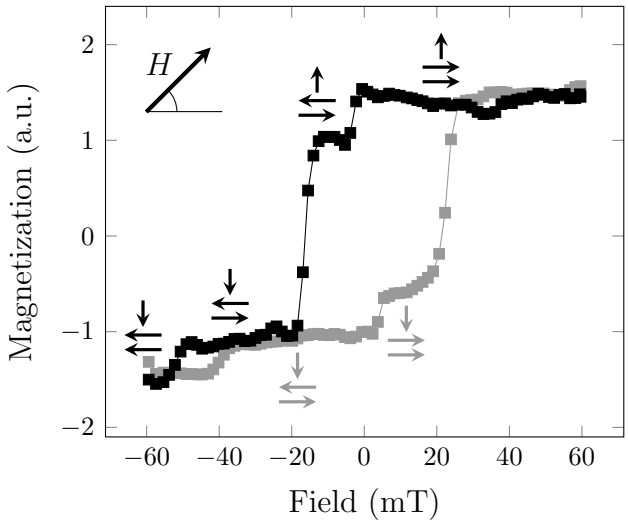

Figure 6.6: Hysteresis loop measured in the in-plane setup. The large step corresponds to switching of the out-of-plane layer, the two smaller steps to the in-plane layers.

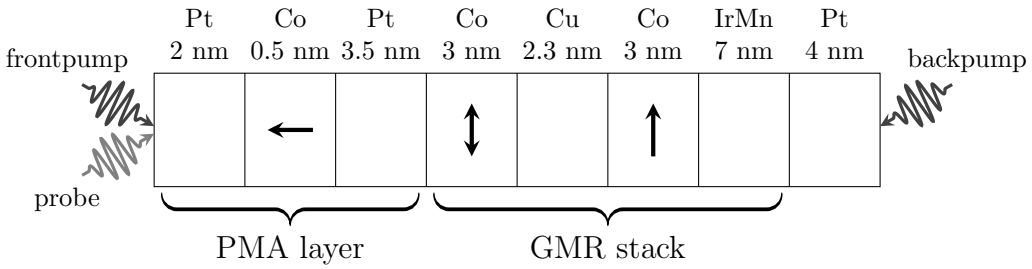

Figure 6.7: Layout of the device. Thick black arrows show the magnetization direction of the magnetic layers.

Finally, Fig. 6.6 shows the hysteresis loop with the external field placed under an angle of 45° with the sample, allowing both the in-plane and out-of-plane cobalt layers to be switched. When sweeping the external field from positive to negative, we first see a small step, corresponding to a switch of the top in-plane layer, after which we see a large step, corresponding to the out-of-plane layer. Finally, we see the pinned layer switch. This shows that the device can indeed be fixed to each of the four required configurations, i.e. both a parallel and an antiparallel GMR stack, with both an upward and a downward directed out-of-plane layer.

6.2 Measurements

In this section the results will be presented of the measurements on the GMTR device. The device layout is depicted in Fig. 6.7. Measurements can be done both with the pump pulse heating the device from the front or from the back, which are referred to as the frontpump and backpump setup respectively. Any measured change in magnetization is assumed to stem purely from the top layer, since in-plane cobalt has a relatively high Curie temperature, and therefore shows no noticeable demagnetization at the laser fluence used in the measurements.

In order to measure the desired effect, both methods discussed in section 3.2.2 were used. As it turns out, only the field modulation method is suitable to measure the effect. These results will be presented first. Then, all measurements using the chopper modulation scheme are presented, together with a discussion why this method is unsuitable to investigate the GMTR effect.

It is important to note that all fields mentioned from now on only correspond to approximately the exact field. The reason for this is that both the strength of the magnet and the angle under which the field is applied change in subsequent measurements, and no effort was done to recalibrate the magnet before each mea-

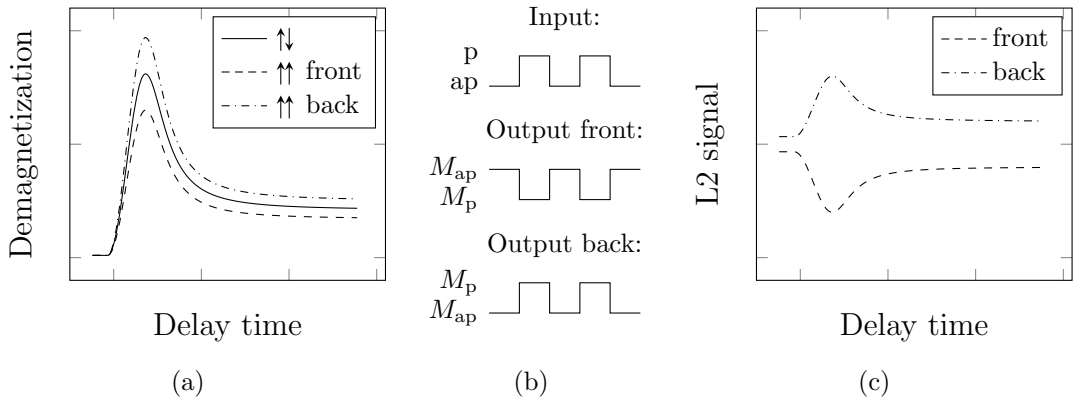

Figure 6.8: (a) Expected demagnetization curves for both the front- and backpump setup. (b) Resulting second lock-in input and output in case the field is modulated to switch one of the in-plane layers. Since the input causes the GMR stack to switch between parallel and antiparallel, the output will either be positive or negative, depending on the setup. (c) Resulting signal for both setups. Demagnetization in (a) is chosen to give a positive signal so that the resulting sign of the effect in (c) is consistent with chapter 5.

surement. Instead, hysteresis loops were measured each time, so that there is still no doubt of the magnetization direction of each layer.

6.2.1 Field Modulation

First, the measurements done using the field modulation method will be presented. All measurements done using this method were done in the polar MOKE setup, which is mostly sensitive to the out-of-plane component of the magnetization. This makes the switching fields of the in-plane layers undetectable, but does increase accuracy.

Using the field modulation method, the field can be adjusted to isolate contributions from switching a single layer. Figure 6.8 shows the expected signal when one of the in-plane layers is switched by the modulation field. Although it is arbitrary whether the demagnetization results in an increase or decrease of the signal — depending on both the magnetization direction and the phase of the lock-in — the GMTR signal is expected to go the opposite direction of the demagnetization signal for the frontpump setup, and the same direction for the backpump setup.

However, since the field has to be applied in-plane to switch the GMR stack, it will change the magnetization direction of the out-of-plane layer. This can

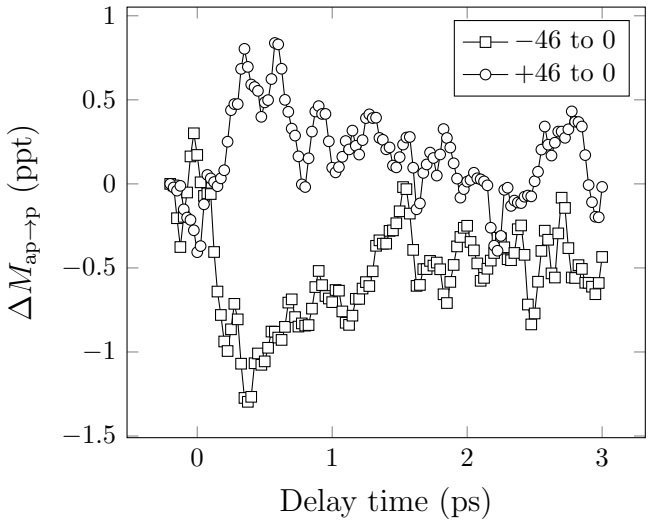

Figure 6.9: Measured signal when modulating the field between 0 and either −46 or +46 mT in percentages of M_{sat}. Since both measurements show a time dependent signal while the pinned layer is switched by only one of the fields, no information can be gained from this measurement.

be seen in Fig. 6.9. Shown here are two measurements in the backpump setup, where the field is modulated between 0 and either −46 or +46 mT. The goal of modulating between 0 and −46 mT is to switch the pinned bottom cobalt layer, without altering the top in-plane and the out-of-plane layers. This then allows the difference in parallel and antiparallel configuration to be measured.

However, if switching of the pinned layer is responsible for the observed effects, the signal should disappear when modulating between 0 and +46 mT. As can be seen, this is not the case. The reason for this is that the magnetic field influences the out-of-plane layer, pulling it slightly in-plane. Once the sample is heated by the pump pulse, the magnetization changes by a certain amount. However, since the probe pulse is mostly sensitive to the out-of-plane component, a smaller change in magnetization is measured with an applied field, resulting in a pump-dependent signal.

To circumvent this problem, an extra magnet was placed behind the sample with a strength of roughly 50–100 mT to fix the out-of-plane layer, and to prevent possible domain formation. It was verified that the stray fields from this magnet remain almost fully out-of-plane over several centimeters, which is more than the distance from the sample. We therefore assume that our in-plane layers remain mostly uninfluenced by this magnet, and can still be aligned either parallel or

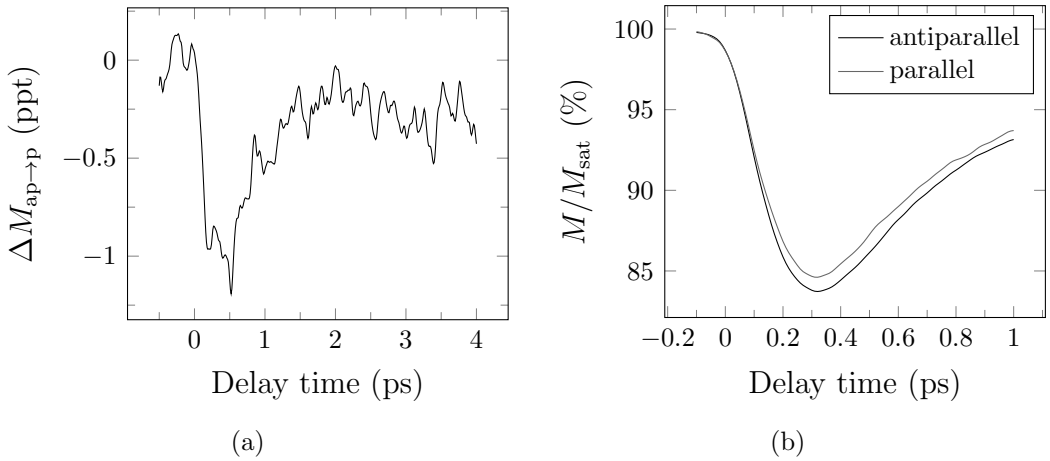

Figure 6.10: (a) Signal measured when modulating between −20 and 20 mT with the out-of-plane layer pinned. (b) Signal measured when modulating between −60 and 60 mT with a free out-of-plane layer (parallel), and the sum of this signal and the one from (a) (antiparallel).

antiparallel. However, this magnet can only be used in the frontpump setup, since it has to be placed close behind the sample.

Figure 6.10 (a) shows the resulting measured curve by modulating between −20 and 20 mT. This signal then gives the change in demagnetization when the GMR stack is switched from antiparallel to parallel alignment. The sign of the signal indeed corresponds to a smaller demagnetization in the parallel configuration, as explained in Fig. 6.8.

Figure 6.10 (b) shows the resulting demagnetization traces for both parallel and antiparallel alignment. The parallel alignment curve was measured by removing the extra magnet, allowing the out-of-plane layer to be switched again, and modulating between −60 and 60 mT. The antiparallel alignment curve was then acquired by adding this signal to the signal from Fig. 6.10 (a). The relative change in demagnetization is then 5.43 %. Comparable values were found from the simulations, but only with the use of a heat sink. Since this is not the case for the measurements, the effect is larger than expected.

However, the question arises whether the measured signal is indeed due to a change in demagnetization. It is unknown if the static magnetic field is strong enough to fix the magnetization direction of the out-of-plane layer. If this would not be the case, other possibilities exist for a measured signal, namely when the magnetization changes (1) due to the modulation field, or (2) due to some sort of coupling with the in-plane layers. Furthermore, there also exists the possibility that (3) the measured

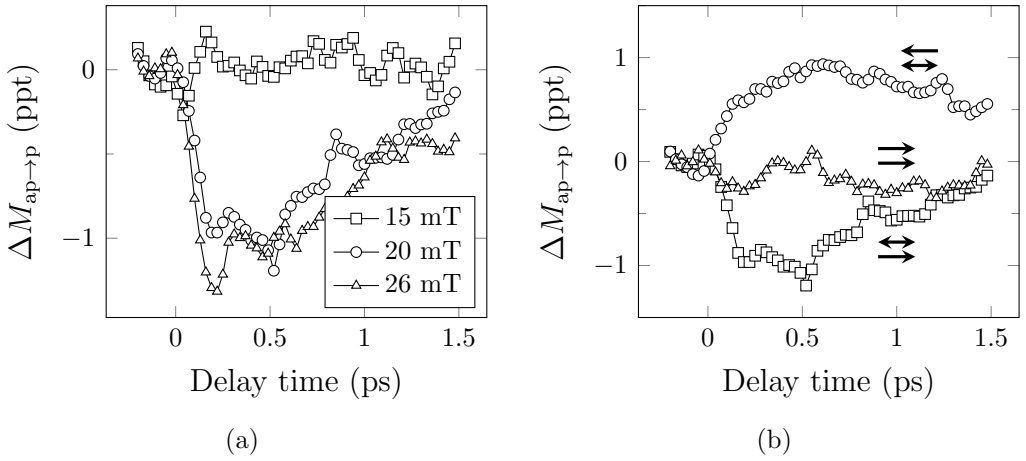

Figure 6.11: (a) Signal for several modulation amplitudes, showing a clear onset of the signal at a certain field. (b) Signal when either the top or the bottom layer is switched, and a reference measurement where no layer is switched. Arrows denote which layer is switched. Modulation used for the top layer is from −20 to 20 mT (−□−), for the bottom from −50 to 0 mT (−○−), and for the reference measurement from +50 to 0 mT (−△−).

signal arises from a change in magnetization of the in-plane layers. In order to confirm that this is not the case, two verifications were done. First of all, the effect was measured at different amplitudes of the field modulation. Figure 6.11 (a) shows a few curves at different modulation amplitudes. At amplitudes of 15 mT or lower, no signal was measured. This corresponds to a minimum field required to switch the in-plane layer. Furthermore, at 20 and 26 mT the size of the effect is of approximately the same strength. This confirms that the measured effect is being caused by switching the GMR stack from parallel to antiparallel, and not due to the magnetic field, excluding possibility (1).

For the second verification the same measurement was done while switching the bottom in-plane layer. This is shown in Fig. 6.11 (b). To switch the bottom layer, the field was modulated between −50 and 0 mT. This gives a change in sign, since the GMR stack is now switched from parallel to antiparallel alignment, opposite to the other measurements. In order to verify that the acquired signal is due to the bottom layer switching, a reference measurement was done while modulating from +50 to 0 mT, which indeed shows no signal. As can be seen, switching either the top or bottom layer gives approximately the same size of effect. Since the bottom layer is placed further away, this excludes possibilities (2) and (3), since these would both result in a smaller measured signal when switching the bottom layer instead of the top layer. There is thus no sign of any signal being

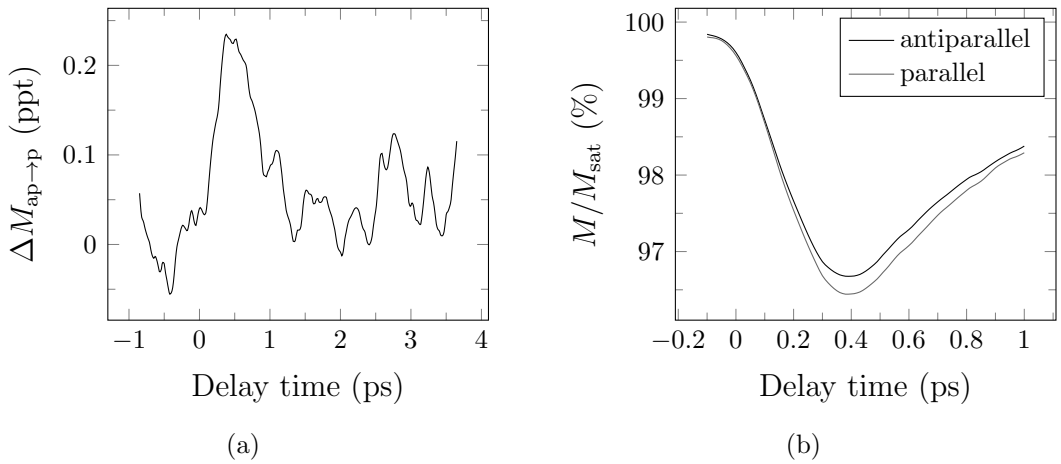

Figure 6.12: (a) Difference in demagnetization from switching the GMR stack in the backpump, and (b) resulting demagnetization curves in the antiparallel and parallel configurations.

measured from the in-plane layers, nor from a change in magnetization direction of the out-of-plane layer, confirming that the measured signal is due to a change in the demagnetization.

The resulting demagnetization traces can be fitted and deconvolved in a similar fashion as done in section 4.1. This gives a demagnetization time of 73 ± 3 fs for both configurations. Within the uncertainty these demagnetization times are exactly the same, which is also the case for the simulations. This provides a nice comparison with the experiment by Malinowski *et al.*[12] whose results were shown in section 1.2, where a comparable device was used. However, in their case the antiparallel alignment provided a channel of angular momentum dissipation, resulting in both a larger and significantly faster demagnetization. This is not the case in our experiment since the magnetization of the GMR stack is now perpendicular to that of the demagnetized material, resulting in only an increase in demagnetization, but no significant difference in demagnetization times.

Finally, some measurements were done with this method in the backpump setup. However, since the laser has to reach both sides of the sample, no static out-of-plane magnetic field could be applied over the sample. The resulting curves are presented in Fig. 6.12. Since the coercivities of the in-plane and out-of-plane layers are of comparable size, only a small range of fields could be used. Therefore no checks could be done to see if the difference is indeed due to the GMTR effect. However, since the field is modulated around zero, no other effects are expected to show a signal. It is therefore assumed that this signal arises due to the GMTR

effect. If this is indeed the case, the backpump setup gives a relative increase in demagnetization when switching to the parallel configuration of 7.02 %, which is slightly larger than in the frontpump setup.

To conclude, it was proven that the demagnetization can be influenced by altering the heat conduction of the device using a GMR stack. However, since only a few measurements could be done, no quantitative insight could be gained into how large a role transport plays for these devices, and how well this can be simulated using the techniques described in chapter 5.

6.2.2 Chopper Modulation

In the following part measurements will be shown using the chopper modulation scheme. The magnetization is now measured using longitudinal MOKE, which has a sensitivity for both the in-plane and the out-of-plane component. Although the sensitivity for the out-of-plane layer is lower than with polar MOKE, this does make the in-plane layers visible, accommodating for easier switching of the GMR stack. Furthermore, the field is placed under an angle with respect to the sample in order to be able to switch all three layers. This angle is approximately 45°.

A similar device as depicted in Fig. 6.7 is used, but with an extra copper layer with a thickness varying between 0 an 10 nm placed between the GMR stack and the PMA layer to act as a heat sink.

Figure 6.13 shows the resulting demagnetization curves in the backpump setup for five different copper heat sink thicknesses. The total demagnetization is small, but this is because the pump pulse has to heat through the thick iridium manganese layer at the bottom. Notably, the total demagnetization deviates considerably between subsequent measurements. This is attributed to the relatively small demagnetization, making small misalignments in the setup much more significant.

There seems to be a tendency for the demagnetization to be larger when the GMR stack is aligned parallel. However, this difference is barely larger than the noise, and much smaller than the difference measured using the field modulation method. This is assumed to be due to this setup being unsuitable to measure the effect. The reason for this is that the out-of-plane layer is susceptible to thermal fluctuations due to its relatively low Curie temperature. Therefore, constant heating from the pump beam in combination with the magnetic field pulling the layer in the wrong direction in some configurations will make this layer unstable. Since the signal is relatively small, long measuring sequences were needed which were then averaged. During these long sequences there was a considerable drift in the measured values,

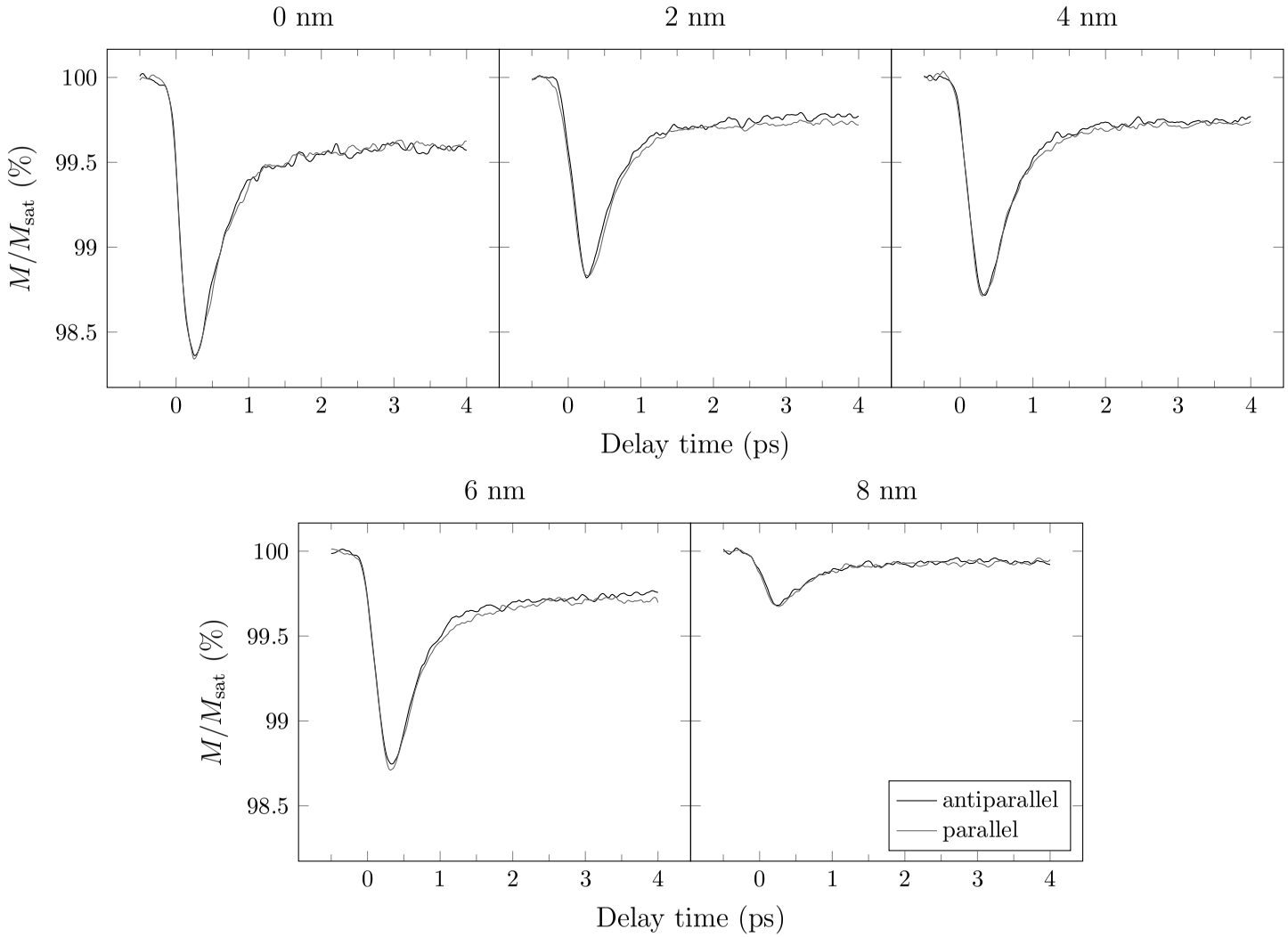

Figure 6.13: Demagnetization in both parallel and antiparallel configuration for 5 different Cu heat sink thicknesses.

presumably due to this instability. Therefore distinguishing the small difference between parallel and antiparallel configuration is nearly impossible.

To conclude this chapter, the influence of the GMTR effect on the demagnetization has been measured. It has been shown that it is possible to influence the demagnetization process by controlling heat transport through the device, and the GMTR effect has been shown to be present on sub-picosecond timescales. The effect was measured in both the front- and backpump setup. For the frontpump setup it has been confirmed that the measured signal arises purely from the GMTR effect, although this was not possible for the backpump setup due to the irreproducibility of the signal at different fields.

Chapter 7

Conclusions and Outlook

In this chapter all important conclusions drawn from measurements and simulations in the previous chapters will be summarized. The conclusions are divided into two parts. In the first part, the conclusions are presented regarding the contribution of superdiffusive spin transport to laser-induced demagnetization of a thin film. The second part shows the conclusions regarding the control of heat transport on ultrafast timescales using a spin-valve. Finally, a few suggestions are given for further research on the subject.

7.1 Conclusions

7.1.1 Spin Transport

The first measurements shown in this thesis were done to investigate whether spin transport can have a large influence on the demagnetization process. The first system investigated consisted of a nickel wedge grown on top of an insulating substrate. The demagnetization was measured for several thicknesses while heating from either the front or the back, allowing a distinction to be made between a demagnetization caused by local heating or by superdiffusive spin transport. This immediately showed that a demagnetization is present throughout the entire device, and that spin transport is not the dominant mechanism. All results found agreed with a theory of local demagnetization within the uncertainty of the measurements.

Next, measurements were done on a nickel layer grown on top of an aluminum film. The presence of this conducting layer should enhance the demagnetization

process according to the superdiffusive model. The measurements again showed a good agreement with the theory of a local demagnetization, and no signs of spin transport were found. However, only thin conducting layers of up to 7 nm of aluminum could be measured, presumably due to growth problems. This is considerably less than the 30 nm used in the predictions by Battiato *et al.*, which could be the reason that no different behavior is observed. Furthermore, all subsequent measurements show significant deviations due to misalignments. Therefore spin transport can only be excluded to be dominant over loss of spin momentum, but it can not be excluded to have any influence.

7.1.2 Heat Transport

Next, it was investigated whether heat transport can be controlled on sub-picosecond timescales using a spin-valve structure. This was first investigated with simulations, showing that a measurable effect is expected. Next, device parameters were optimized, after which a working device has been fabricated. The effect has been investigated using two different measuring methods, of which only one was shown to be suitable to measure the effect.

Using this method, a change in demagnetization due to the GMTR effect has been measured. It was verified that the measured signal indeed resulted from the change in heat conduction, and not from other effects. With these measurements it was for the first time demonstrated that ultrafast heat transport can be controlled using a magnetic field, opening up new possibilities for future devices as a method to investigate the interplay between the charge and spin degrees of freedom on ultrafast timescales.

Finally, some measurements were presented in the backpump setup with this method. However, since this setup did not allow for an extra magnetic field to be applied to stabilise the out-of-plane layer during the in-plane field modulation, we are uncertain how reliable these measurements are.

7.2 Outlook

Although this thesis provides a proof of principle, no quantitative conclusions could be drawn due to the effect being relatively small. By increasing the measured effects, perhaps more can be said about both the GMTR effect and the types of transport present in these devices. Increasing the effect should be possible, since the measured devices only showed a CIP MR ratio of approximately 2.5 %, while 8–10 % has been shown to be achievable in similar devices.

Another way to increase the effect is to use multilayered GMR stacks coupled through the RKKY interaction, in which the amount of layers used provides an extra degree of optimization. Furthermore, these generally grow well on top of copper, allowing the use of a heat sink, which is expected from simulations to greatly increase the effect.

Furthermore, for the device used in this thesis not much was known about the strength of the GMTR effect under equilibrium conditions. The exact size of the effect could therefore also be investigated in the materials used for our devices. This could help improve the parameters used in the simulations, possibly allowing for better distinction between different models used.

Finally, for the measurements done on spin transport, the influence of a conducting bottom layer were investigated. However, only layer thickness of up to 7 nm were used in the measurements, while all predictions of the superdiffusive model were made using layer thicknesses of 30 nm, which could make a significant difference. Although this has been excluded to be the dominant mechanism, it is interesting to investigate whether it could still provide a small influence.

Bibliography

[1] H. Coufal and L. Dhar andC.D. Mee. "Materials for magnetic data storage: the ongoing quest for superior magnetic materials," *MRS Bulletin* **31**, 374 (2006).

[2] S.S.P. Parkin, K.P. Roche, M.G. Samant, P.M. Rice, R.B. Beyers, R.E. Scheuerlein, E.J. O'Sullivan, S.L. Brown, J. Bucchigano, D.W. Abraham, Yu Lu, M. Rooks, P.L. Trouilloud, R.A. Wanner, and W.J. Gallagher. "Exchange-biased magnetic tunnel junctions and application to nonvolatile magnetic random acces memory," *Journal of Applied Physics* **85**, 5828 (1999).

[3] S.S.P. Parkin, M. Hayashi, and L. Thomas. "Magnetic domain-wall racetrack memory," *Science* **320**, 190 (2008).

[4] T. Devolder and C. Chappert. "Precessional switching of thin nanomagnets: analytical study," *European Physical Journal B* **36**, 57 (2003).

[5] H.W. Schumacher, C. Chappert, P. Crozat, R.C. Sousa, P.P. Freitas, J. Miltat, J. Fassbender, and B. Hillebrands. "Phase coherent precessional magnetization reversal in microscopic spin valve elements," *Physical Review Letters* **90**, 017201 (2003).

[6] A.A. Tulapurkar, T. Devolder, K. Yagami, P. Crozat, C. Chappert, A. Fukushima, and Y. Suzuki. "Subnanosecond magnetization reversal in magnetic nanopillars by spin angular momentum transfer," *Applied Physics Letters* **85**, 5358 (2004).

[7] T.A. Ostler, J. Barker, R.F.L. Evans, R.W. Chantrell, U. Atxitia, O. Chubykalo-Fesenko, S. El Moussaoui, L. Le Guyader, E. Mengotti, L.J. Heyderman, F. Nolting, A. Tsukamoto, A. Itoh, D. Afanasiev, B.A. Ivanov, A.M. Kalashnikova, K. Vahaplar, J. Mentink, A. Kirilyuk, Th. Rasing, and A.V. Kimel. "Ultrafast heating as a sufficient stimulus for magnetization reversal in a ferrimagnet," *Nature Communications* **3**, 666 (2012).

[8] E. Beaurepaire, J.-C. Merle, A.Daunois, and J.-Y. Bigot. "Ultrafast spin dynamics in ferromagnetic nickel," *Physical Review Letters* **76**(22), 4250 (1996).

[9] B. Koopmans, G. Malinowski, F. Dalla Longa, D. Steiauf, M. Fähnle, T. Roth, and M. Cinchetti. "Explaining the paradoxical diversity of ultrafast laser-induced demagnetization," *Nature Materials* **9**, 259 (2010).

[10] M. Battiato, K. Carva, and P.M. Oppeneer. "Superdiffusive spin transport as a machanism of ultrafast demagnetization," *Physical Review Letters* **105**, 027203 (2010).

[11] M. Battiato, K. Carva, and P.M. Oppeneer. "Theory of laser-induced ultrafast superdiffusive spin transport in layered heterostructures," *Physical Review B* **86**, 024404 (2012).

[12] G. Malinowski, F. Dalla Longa, J.H.H. Rietjens, P.V. Paluskar, R. Huijink, H.J.M. Swagten, and B. Koopmans. "Control of speed and efficiency of ultrafast demagnetization by direct transfer of spin angular momentum," *Nature Physics* **4**, 858 (2008).

[13] C. Kittel. *Introduction to Solid State Physics*. John Wiley & Sons, Inc, (2005).

[14] H.J.M. Swagten. *Magnetism and Magnetic Materials*. (2010). 3S100 course syllabus 2010–2011.

[15] R.J. Elliot. "Theory of the effect of spin-orbit coupling on magnetic resonance in some semiconductors," *Physical Review* **96**, 266 (1954).

[16] F. Dalla Longa. *Laser-induced magnetization dynamics*. PhD thesis, Eindhoven University of Technology, (2008).

[17] B. Koopmans, G. Malinowski, F. Dalla Longa, D. Steiauf, M. Fähnle, T. Roth, and M. Cinchetti. Supplementary information in *Nature Materials* **9**, 259.[9]

[18] N.F. Mott. "The electrical conductivity of transition metals," *Proceedings of the Royal Society of London* **153**, 699 (1936).

[19] J. Sólyom. *Fundamentals of the Physics of Solids*, volume 2. Springer, (2008).

[20] H. Ibach and H. Lüth. *Solid-State Physics*. Springer, (2003).

[21] T. Jeong. *Spin-dependent heat transport and thermal boundary resistance*. PhD thesis, Carnegie Mellon University, (2011).

[22] J. Shi, K. Pettit, E. Kita, S.S.P. Parkin, R. Nakatani, and M.B. Salamon. "Field-dependent thermoelectric power and thermal conductivity in multilayered and granular giant magnetoresistive systems," *Physical Review B* **54**, 15273 (1996).

[23] Y. Yang, G.-G. Zhu, R.M. White, and M. Asheghi. "Field-dependent thermal and electrical transport in Cu/CoFe multilayer," *Journal of Applied Physics* **99**, 063703 (2006).

[24] R. Metzler and J. Klafter. "The random walk's guide to anomalous diffusion: a fractional dynamics approach," *Physics Report* **339**, 1 (2000).

[25] C.A. Schmuttenmaer, M. Aeschlimann, H.E. Elsayed-Ali, R.J.D. Miller, D.A. Mantell, J. Cao, and Y. Gao. "Time-resolved two-photon photoemission from Cu(100): Energy dependence of electron relaxation," *Physical Review B* **50**, 8957 (1994).

[26] R. Knorren, K.H. Bennemann, R. Burgermeister, and M. Aeschlimann. "Dynamics of excited electrons in copper and ferromagnetic transition metals: Theory and experiment," *Physical Review B* **61**, 6427 (2000).

[27] E. Knoesel, A. Hotzel, T. Hertel, M. Wolf, and G. Ertl. "Dynamics of photoexcited electrons in metals studied with time-resolved two-photon photoemission," *Surface Science* **368**, 76 (1996).

[28] L.A.A. Pettersson, L.S. Roman, and O. Inganäs. "Modeling photocurrent action spectra of photovoltaic devices based on organic thin films," *Journal of Applied Physics* **1**, 487 (1999).

[29] D.J. Griffiths. *Introduction to Electrodynamics*. Pearson, (2008).

[30] C. Józsa. *Optical detection of the magnetization precession*. PhD thesis, Eindhoven University of Technology, (2006).

[31] M. van Kampen. *Ultrafast spin dynamics*. PhD thesis, Eindhoven University of Technology, (2003).

[32] R.L. Fork. "Negative dispersion using pairs of prisms," *Optics Letters* **9**(5), 150 (1984).

[33] Stanford Research Systems. "About Lock-In Amplifiers," (2012).
URL: `http://www.thinksrs.com/downloads/PDFs/ApplicationNotes/AboutLIAs.pdf`

[34] A.J. Schellekens, W. Verhoeven, T.N. Vader, and B. Koopmans. "Investigating the contribution of superdiffusive transport to ultrafast demagnetization of ferromagnetic thin films," *Applied Physics Letters* **102**, 252408 (2013).

[35] T.N. Vader. *Heat and spin transport in ultrafast magnetization dynamics*. Master's thesis, Eindhoven University of Technology, (2012).

[36] J.H.H. Rietjens. *Spin dynamics in hybrid spintronic devices and semiconductor nanostructures*. PhD thesis, Eindhoven University of Technology, (2009).

[37] M.D. Stiles. "Spin–dependent interface transmission and reflection in magnetic multilayers," *Journal of Applied Physics* **79**, 5805 (1996).

[38] P. Janssen. *The nanostencil process*. Master's thesis, Eindhoven University of Technology, (2008).

[39] B. Dieny, V.S. Speriosu, S. Metin, S.S.P. Parkin, B.A. Gurney, P. Baumgart, and D.R. Wilhoit. "Magnetotransport properties of magnetically soft spin-valve structures," *Journal of Applied Physics* **69**, 4774 (1991).

[40] Th.G.S.M. Rijks. *Layered thin films for sensor applications: magnetoresistance and magnetic interactions*. PhD thesis, Eindhoven University of Technology, (1996).

[41] M. Ali, C.H. Marrows, M. Al-Jawad, and B.J. Hickey. "Antiferromagnetic layer thickness dependence of the IrMn/Co exchange bias system," *Physical Review B* **68**, 214420 (2003).

[42] I.L. Prejbeanu, W. Kula, K. Ounadjela, R.C. Sousa, O. Redon, B. Dieny, and J.-P. Nozières. "Thermally assisted switching in exchange-biased storage layer magnetic tunnel junctions," *IEEE Transactions on Magnetics* **40**, 2625 (2004).

[43] J.P. Nozières, S. Jaren, Y.B. Zhang, A. Zeltser, K. Pentek, and V.S. Speriosu. "Blocking temperature distribution and long-term stability of spin-valve structures with Mn-based antiferromagnets," *Journal of Applied Physics* **87**(8), 3920 (2000).

[44] J. van Driel and F.R. de Boer. "Exchange biasing by $Ir_{19}Mn_{81}$: dependence on temperature, microstructure and antiferromagnetic layer thickness," *Journal of Applied Physics* **88**(2), 975 (2000).

[45] A.J. Devasahayam and M.H. Kryder. "The dependence of the antiferromagnet/ferromagnet blocking temperature on antiferromagnet thickness and deposition conditions," *Journal of Applied Physics* **85**(8), 5519 (1999).

[46] E. Kerr, S. van Dijken, and J.M.D. Coey. "Influence of the annealing field strength on exchange bias and magnetoresistance of spin valves with IrMn," *Journal of Applied Physics* **97**, 093910 (2005).

[47] P.F. Carcia. "Perpendicular magnetic anisotropy in Pd/Co and Pt/Co thin-film layered structures," *Journal of Applied Physics* **63**, 5066 (1988).